

©2016, Elsevier. Licensed under the Creative Commons Attribution-NonCommercial-NoDerivatives 4.0 International <http://creativecommons.org/about/downloads>



Discriminating fluid source regions in orogenic gold deposits using B-isotopes

James S. Lambert-Smith^{a*}, Alexander Rocholl^b, Peter J. Treloar^a and David M. Lawrence^c

^aSchool of Geography, Geology and the Environment, Kingston University London, Kingston upon Thames,

KT1 2EE, UK

^bHelmholtz Centre Potsdam, GFZ German Research Centre for Geosciences, Telegrafenberg, D14473

Potsdam, GERMANY

^cRandgold Resources Ltd, Unity Chambers, Halkett Street, St Helier, Jersey, JE2 4WJ, UK

***Corresponding author email address: J.S.Lambert-Smith@kingston.ac.uk**

¹Non-standard abbreviation: Senegal-Mali Shear Zone - SMSZ

Abstract

The genesis of orogenic gold deposits is commonly linked to hydrothermal ore fluids derived from metamorphic devolatilisation reactions. However, there is considerable debate as to the ultimate source of these fluids and the metals they transport. Tourmaline is a common gangue mineral in orogenic gold deposits. It is stable over a very wide *P-T* range, demonstrates limited volume diffusion of major and trace elements and is the main host of B in most rock types. We have used texturally resolved B-isotope analysis by Secondary Ion Mass Spectrometry (SIMS) to identify multiple fluid sources within a single orogenic gold ore district. The Loulo Mining District in Mali, West Africa hosts several large orogenic gold ore bodies with complex fluid chemistry, associated with widespread pre-ore Na- and multi-stage B-metasomatism. The Gara deposit, as well as several smaller satellites, formed through partial mixing between a dilute aqueous-carbonic fluid and a hypersaline brine. Hydrothermal tourmaline occurs as a pre-ore phase in the matrix of tourmalinite units, which host mineralisation in several ore bodies. Clasts of these tourmalinites occur in mineralised breccias. Disseminated hydrothermal and vein hosted tourmaline occur in textural sites which suggest growth during and after ore formation. Tourmalines show a large range in $\delta^{11}\text{B}$ values from -3.5 to 19.8 ‰, which record a change in fluid source between paragenetic stages of tourmaline growth. Pre-mineralization tourmaline crystals show heavy $\delta^{11}\text{B}$ values (8 to 19.8 ‰) and high X-site occupancy (Na \pm Ca; 0.69 to 1 apfu) suggesting a marine evaporite source for hydrothermal fluids. Syn-mineralization and replacement phases show lighter $\delta^{11}\text{B}$ values (-3.5 to 15.1 ‰) and lower X-site occupancy (0.62 to 0.88 apfu), suggesting a subsequent influx of more dilute fluids derived from devolatilisation of marine carbonates and clastic metasediments. The large, overlapping range in isotopic compositions and a skew toward the opposing population in the $\delta^{11}\text{B}$ data for both tourmaline groups reflects continual tourmaline growth throughout mineralisation, which records the process of fluid mixing. A peak in $\delta^{11}\text{B}$ values at ~ 8 ‰ largely controlled by tourmalines of syn- to post-ore timing represents a mixture of the two isotopically distinct fluids. This paper demonstrates that B-isotopes in tourmaline can be instrumental in interpreting complex and dynamic hydrothermal systems. The importance of B as an integral constituent of orogenic ore forming fluids and as a gangue phase in orogenic gold deposits makes B-isotope analysis a powerful tool for testing the level of source region variability in these fluids, and by extension, that of metal sources.

1. Introduction

Orogenic gold deposits are one of the most important contributors of new gold to the market, accounting for 30 % of total past production, reserves, and resources (Frimmel and Hennigh, 2015). In a series of seminal papers Groves and colleagues (Groves et al., 1998; Goldfarb et al. 2001; Groves et al., 2003; Groves et al., 2005) defined the model for orogenic gold and identified the tectonic settings within which they occur. This model has since seen refinement (Phillips and Powell, 2009; Phillips and Powell, 2010), but a suite of geological similarities has remained more or less consistent: 1) an intimate association with orogenic events; 2) a strong structural control on the location of ore bodies at a variety of scales; 3) ore bodies commonly developed syn- to post-peak metamorphism in greenschist facies terranes; 4) wall rock alteration dominated by carbonate, mica, (\pm albite), chlorite, quartz, and pyrite; 5) aqueous-carbonic (5-30 mole % $\text{CO}_2 \pm \text{CH}_4 \pm \text{N}_2$) ore fluids, with uniformly low salinities (<6 wt. % NaCl equiv.), and near neutral pH. Almost every other aspect of orogenic gold deposits is highly variable (age, host terrane, mineralogy etc.).

Despite these well-established characteristics, there remains considerable debate as to the ultimate source of orogenic gold ore fluids and the metals that they transport (Tomkins, 2013; Goldfarb and Groves, 2015; Wyman et al., 2016). The most favoured candidate fluid sources are: 1) metamorphic devolatilisation (Kerrick and Wyman, 1990; Goldfarb et al., 1991; Phillips, 1993; McCuaig and Kerrich, 1998; Yardley and Cleverly, 2013); and 2) hydrothermal fluids exsolved from crystallising magmas (de Ronde et al., 2000; Lawrence et al., 2013a; Lawrence et al., 2013b; Treloar et al., 2014). However, alternate sources have been suggested, including, deeply convecting meteoric water (Hagemann et al., 1994; Jenkin et al., 1994), mantle-sourced fluids (Cameron, 1988; Hronsky et al., 2012), or fluids expelled from subducting oceanic crust (Breeding and Ague, 2002). In general, candidate sources of Au share similarities with those of fluids. These include leaching of metals from metamorphosing rocks (Phillips and Powell, 2010), primary magmatic sources (Lawrence et al., 2013a; Lawrence et al., 2013b; Treloar et al., 2014), or a mantle source (Hronsky et al., 2012). While metamorphic devolatilisation has become increasingly favoured as both a fluid and metal source (Tomkins, 2013), debate continues as to the nature of the source region. Emphasis is variably placed on either 'pre-enrichment' of particularly favourable source rocks (e.g. Large et al., 2011; Gaboury, 2013), or on leaching of large volumes of crust with background levels of Au enrichment (Phillips and Powell, 2010; Wilson et al., 2013; Pitcairn et al., 2014a; Pitcairn et al., 2014b).

As an example of this debate, Gaboury, (2013) and Xue et al. (2013) presented compelling, but conflicting, evidence for auriferous ore fluids being sourced from carbonaceous shales and from felsic magmas, respectively. Both studies were carried out on greenstone hosted orogenic gold deposits of similar age, but utilising different analytical datasets, which are thus difficult to compare (residual gas analysis of fluid inclusions and multiple sulphur isotopes, respectively). The comparison of such studies raises fundamental questions as to whether the sources of ore fluids and metals in orogenic gold deposits are simply extremely difficult to trace precisely, or if there is indeed high variability in their source regions and processes. In order to address this key question, it is necessary to employ a robust method of fingerprinting fluid sources; one which can ideally be applied across the varied spectrum of orogenic-style Au deposits. Recent work by Garofalo et al. (2014) reinforced the apparently homogenous nature of the mineralising fluids associated with orogenic gold, noting that they are also uniformly enriched in Au, As, Sb and B.

Tourmaline is a common gangue mineral in orogenic gold deposits (Groves et al., 1998; Beaudoin and Pitre, 2005; Jiang et al., 2002; Krienitz et al., 2008; Garofalo et al., 2014). It is stable over a very wide *P-T* range, making it resistant to post-depositional modification (Dutrow and Henry, 2011). This, combined with extremely limited volume diffusion of major and trace elements below 600°C, means that isotopic ratios recorded in tourmaline are typically extremely well preserved (van Hinsberg et al., 2011a). Tourmaline is the main host of boron in most rock types. Because the range in boron isotopic composition observed in tourmaline is far larger than can be explained by temperature or pH controlled isotopic fractionation (Palmer and Slack, 1989), the ratio between ¹¹B and ¹⁰B (commonly expressed as δ¹¹B units) is an excellent indicator of the fluid source; especially where some estimate of temperature can be made. It is for these reasons that the use of stable B-isotopes in tourmaline has become well established in the study of ore deposits (e.g. Palmer and Slack, 1989; Xavier et al., 2008; Garda et al., 2009; Slack and Trumbull, 2011; Tornos et al., 2012; Duncan et al., 2014; Molnár et al., 2016). While boron isotope analysis by thermal ionization mass spectrometry (TIMS) requires complete chemical dissolution of a bulk tourmaline sample, secondary ion mass spectrometry (SIMS) allows for texturally resolved measurement of δ¹¹B in tourmaline at levels of precision that allow detailed analysis of fluid source reservoirs in relation to the mineral paragenesis.

Here we demonstrate the robust nature of texturally resolved B-isotope SIMS analysis to identify multiple

fluid sources within a single orogenic Au district. The Loulo Mining District in Mali, West Africa hosts several large (>3 Moz) orogenic Au ore bodies with unusually complex fluid chemistry (Lawrence et al., 2013a; Lawrence et al., 2013b). The Gara deposit, as well as several smaller satellites, formed due to partial mixing between a dilute aqueous-carbonic fluid and a hypersaline brine. Lawrence et al. (2013b) interpreted the aqueous-carbonic fluid to be of metamorphic origin. The brine was interpreted to have been derived from either evaporitic source rocks or from magmatism. The debate articulated by Lawrence et al. (2013b) goes to the core of the argument about potential sources of ore bearing fluids in orogenic gold systems. Our new $\delta^{11}\text{B}$ data reveal the hypersaline fluid to be derived from a meta-evaporite reservoir. Furthermore, our in-situ $\delta^{11}\text{B}$ data on individual tourmaline grains record changes in fluid source between different paragenetic stages of tourmaline growth. This study will thus emphasise the strength of tourmaline B-isotopes in fingerprinting fluid sources, and ultimately, metal sources, particularly in orogenic gold systems in which B is clearly a common constituent (Garofalo et al., 2014).

2. Geological setting

The West African Craton can be divided into three domains: 1) the Reguibat Rise in Mauritania, Morocco and western Algeria; 2) the Leo-Man Rise in sub-Saharan West Africa and, 3) The Kayes and Kédougou-Kéniéba Inliers (KKI; this study area) in the Sahel region, North West of the Leo Rise. The Reguibat and Leo shields comprise a western Archaean domain and a central and eastern Palaeoproterozoic (Birimian) domain. The Birimian domain of the Leo-Man Shield is referred to as the Baoulé-Mossi domain (Fig. 1). The Birimian terranes consist of narrow, linear to arcuate, N to NNE trending volcanic belts, separated by broad sedimentary basins. Extensive suites of plutonic rocks intrude both units. The terranes were accreted and cratonised during the Eburnean orogeny, a period of SE to NW directed crustal shortening, metamorphism and magmatic accretion (Oberthür et al., 1998; Feybesse et al., 2006). Peak metamorphic conditions are widely reported as amphibolite facies (500–600°C; 4–6 kbar; John et al., 1999; White et al., 2013), with a retrograde greenschist facies overprint (Hirdes et al., 1996).

The Birimian terranes formed over a period of ~180 Ma (Perrouty et al., 2012; White et al., 2014 and references therein; Parra-Avila et al., 2015). This period is divided into two phases. Though there is regional variation, broadly the Eoeburnean (also known as Eburnean I or the Tangaeen; 2266–2150 Ma) precedes the

Eburnean (2216-1980 Ma) (Taylor et al., 1992; Dia et al., 1997; Loh et al., 1999; Allibone et al., 2002; Gueye et al., 2007; Tshibubudze et al., 2009; Hein, 2010; de Kock et al., 2011). The Eoeburnean consists of volcanism, granitoid emplacement and fold, thrust tectonics, and is interpreted by Tshibubudze et al., (2015) to be a single diachronous event across the Birimian. This is followed by emplacement of younger granitoid plutons, strike-slip deformation and mineralisation in the Eburnean. U-Pb dating of detrital zircons suggests that sedimentary basins developed toward the end of Eoeburnean into the Eburnean; oldest detrital zircons range from 2165 to 2080 Ma across the Baoulé-Mossi domain (Oberthür et al., 1998; Davis et al., 1994; Hirdes and Davis et al., 2002; Vidal et al., 2009).

3. The Loulo Mining District

3.1. Local Geology

The Au deposits studied here belong to the Loulo Mining District in the KKI (Fig. 2a). Au reserves of 7.8 Moz and 630 Mt of Fe ore are hosted along the Senegal-Mali Shear Zone (SMSZ; Fig. 2a and b). West of the SMSZ, Fe is hosted in a series of skarn deposits (Schwartz and Melcher, 2004) in the Falémé Volcanic Belt (FVB). In the Loulo Mining District to the east of the SMSZ Au mineralization is hosted in the Kofi Series (2.09 to 2.04 Ga) (Bassot and Cean-Vachette, 1984; Boher et al., 1992) at the Gara, Yalea and Goukoto mines.

The FVB is a north-northeast trending belt of high-K calc-alkaline volcanic and plutonic rocks (Lambert-Smith et al., 2016a). The plutonic rocks comprise dioritic to granodioritic porphyry complexes, with an outcrop area in excess of 300 km² (Fig. 2b). The volcanic sequences comprise pillowed andesite flows, subordinate rhyodacite lavas and pyroclastic rocks. These are interbedded with volcanoclastic rocks, wackes and carbonate lithologies (Hirdes and Davis, 2002; Schwartz and Melcher, 2004). Magnetite skarn deposits are hosted in several of the smaller plutons and carbonate wall rocks (Schwartz and Melcher, 2004).

The Kofi Series comprises metamorphosed immature detrital sedimentary and carbonate rocks, and breccias, intruded by minor mafic dykes and small intermediate to felsic stocks. The sedimentary rocks in the Kofi Series are dominantly wackes. These are comprised of sandstone and argillite, interbedded on a cm scale. Both rock types also occur as metric scale units, with gradational changes from quartz wacke through to argillite. The siliciclastic component of the wackes varies between quartz-rich and feldspar-rich. Crystal clasts show a large range in grain size and shape. The Kofi series becomes more carbonate-rich to the west,

with proximity to the Falémé Volcanic Belt (Fig. 2b). These carbonate rocks are dominantly calcitic, highly deformed, and feature marl horizons; clasts in marls are composed of quartz and feldspars and are typically fine grained and sub angular. All sedimentary lithologies in the Kofi Series have been affected by multiple phases of folding. The igneous rocks, which intrude the Kofi Series, comprise dolerite to monzodiorite dykes and small stocks of quartz-feldspar-phyric rhyolite. Two larger plutons of monzogranite composition, the Gamaye and Yatea plutons, also intrude the Kofi Series (Fig. 2b). The Gamaye pluton has been dated by Rb-Sr analysis at 2045 ± 27 Ma (Bassot and Caen-Vachette, 1984) and no age data currently exists for the Yatea pluton. Certain packages of quartz wacke, particularly in the west of the Kofi Series have been intensely tourmalinised, while others have been albitised (Lawrence et al., 2013a; Fig. 3). Albitization is widespread in the Kofi Series, with several extensive bodies of hydrothermal albitite situated close to the Senegal-Mali Shear Zone (Fig. 2b). These alteration facies reflect a significant flux of Na- and B-rich (hypersaline) fluid through the wall rocks of the SMSZ.

3.2. Previous work

Previous work on the Senegal-Mali Shear Zone and its mineral deposits has largely focused on the Loulo Mine Complex (Dommanget et al., 1993; Fouillac et al., 1993; Lawrence et al., 2013a and b; Lambert-Smith et al., 2016a and b) and a small subset of the Falémé Iron District skarns (Schwartz and Melcher, 2004). Lawrence et al. (2013a and b) focused on the Gara and Yatea deposits (combined reserves of 4.7 Moz at 4.6 g/t) with a detailed petrographic, fluid inclusion and stable isotope (O, C and S) study. The key finding of Lawrence et al. (2013b) was that two distinct hydrothermal fluids contributed to Au mineralization at the Gara deposit.

At Gara, ore is hosted in ankerite-quartz-pyrite veins, developed in a fractured and folded quartz wacke unit that had previously been pervasively tourmalinized (Fig. 3a). A ~50 m envelope of albitization (Fig. 3b) encompasses the ore zone. This is related to a regional-scale pre-ore sodic alteration anomaly developed along the SMSZ. Accessory ore phases at Gara include chalcopyrite, gersdorffite, pentlandite, arsenopyrite, monazite, scheelite and xenotime. Arsenopyrite is scarce in comparison to other orogenic gold deposits hosted in metasedimentary rocks, both within the Birimian and globally (Groves et al., 1998).

The Yatea deposit is hosted in a 10- to 40-m-wide zone of strongly metasomatized (carbonate-albite

followed by sericite-chlorite), brittle-ductile deformed rocks. The north lode of the deposit (Yalea North) shares mineralogical characteristics with Gara. Here tourmaline is present in clasts of tourmalinite as well as crystal clasts and hydrothermal grains in the matrix; arsenopyrite is rare and Ni-Co bearing phases common. In contrast, the Yalea Main ore body is As-rich. Arsenopyrite and arsenian pyrite are the dominant sulphide phases with accessory pyrrhotite, chalcopyrite and tennantite. Alteration assemblages notably lack tourmaline, though sodic, carbonate and phyllic alteration are widespread.

Lawrence et al. (2013b) reported fluid inclusion assemblages at the Gara ore-body that represented two physico-chemically distinct fluids: 1) A high T, high-salinity, aqueous, CO₂-poor fluid (~400°C; ~45-55 wt. % NaCl equiv.; XH₂O of 0.7-0.8; XCO₂ < 0.3); and 2) a lower T, low-salinity, H₂O-CO₂ fluid (270-350°C; <10 wt. % NaCl equiv.; XH₂O of 0.5-0.9; XCO₂ 0.1-0.5). High salinity fluid inclusions contain daughter minerals that include NaCl, FeCl₂, Fe₂O₃, Fe₃O₄ and carbonate minerals. The co-existence of H₂O-CO₂-NaCl inclusions of variable salinity (5-21 wt.% NaCl equiv) and XCO₂ (0.04-0.67; Lawrence et al., 2013b) indicates that partial mixing between the two fluids resulted in retrograde boiling and changes in the physico-chemical state of both fluids (T, *f*O₂, and pH) leading to Au precipitation. This same fluid system is present at Yalea North. However, at Yalea Main the hypersaline fluid is notably absent. Here, fluid inclusion assemblages feature two immiscible phases derived from phase separation in the low salinity H₂O-CO₂ fluid described at Gara. Further work has confirmed the presence of the hypersaline fluids throughout the Loulo Mining District (Lambert-Smith et al., 2016b). However, the formation of large Au deposits in the absence of the brine indicates that the dilute fluid is more important as a carrier of Au, and that the brine provided a localised trapping mechanism (Lambert-Smith et al. 2016b). Lawrence et al. (2013b) suggested the possibility of an evaporite origin for the brines, but ultimately argued for a magmatic source. This argument was based on fluid chemistry (FeCl₂-rich), alteration assemblages (tourmalinization and albitization), and metal content of ores (Fe-REE-P-W-Cu ± Ni ± Co); although stable isotope data (O, C and S) were less conclusive.

4. Tourmaline occurrences and paragenesis

Hydrothermal tourmaline occurs throughout the SMSZ. This manifests as a boron soil chemistry anomaly of >200 ppm, which extends for >150 km along strike of the shear zone (Fig. 4). This affects the area immediately around the Gara and Yalea mines as well as the northern Falémé Belt and extends as far north

as the Sadiola Au deposit (Masurel et al., 2015). Hydrothermal tourmaline occurs in a number of different alteration styles throughout the region, including: 1) tourmalinite units, 2) breccia hosted tourmalinite clasts, and 3) disseminated hydrothermal tourmaline (Lawrence et al., 2013a). Tourmaline of demonstrably primary magmatic origin occurs in pegmatite dykes that cut the Gamaye pluton, which is also associated with anomalous concentrations of B in soils (Fig. 4).

Lawrence et al., (2013a) defined a paragenesis for hydrothermal tourmaline in the SMSZ, with Gara the type locality. This comprises: 1) Pre-mineralization tourmaline (~ 60-75 % of the overall tourmaline); 2) Syn-mineralization tourmaline (5-10 %) and 3) late- to post-ore replacement tourmaline (20-35 %). This paragenesis, while not always complete, is largely applicable throughout the LBD.

Pre-mineralization tourmaline is represented by tourmalinite units, which host mineralization at Gara, the P-64 satellite ore body and the Baqata exploration target. Tourmalinite units are black in colour and are generated through pervasive replacement of the matrix of fine to medium sand layers in quartz wacke units (Fig. 3a). Tourmaline replaces 30-80 % of the rock, is extremely fine grained to cryptocrystalline (<30 µm; Fig. 5a and c), subhedral, and is often intergrown with quartz or chlorite. The presence, regionally of unaltered quartz wacke packages combined with a structural control on the intensity of matrix tourmalinisation confirms that these units are epigenetic and hydrothermal in nature and not related to exhalative processes (Lawrence et al., 2013a). Tourmalinite units host a distinctive ankerite-quartz-pyrite hydro-fracture vein style of mineralization (Fig. 3a and Fig. 5a). Clasts of pre-mineralization tourmalinite frequently occur within hydrothermal breccias at Yalea North (Fig. 5b), constraining breccia hosted mineralisation to after this early tourmalinisation phase.

Syn-mineralization tourmaline occurs within auriferous veins, in narrow alteration halos around veins, and in the matrix of mineralised hydrothermal breccias. At Gara, syn-mineralization tourmaline occurs as <100 µm acicular crystals growing perpendicular to the walls of auriferous carbonate-quartz veins (Fig. 5d **Error! Reference source not found.**). These are interpreted to have grown as the veins were opening and therefore directly coincide with ore deposition. At the Yalea North ore body, clasts of early tourmalinite are present in the breccia, in addition to syn-mineralization tourmaline, which occur in the cement of hydrothermal-tectonic breccias (Fig. 5b). These tourmalines are fine (typically <100 µm), subhedral to

euohedral (hexagonal when viewed along c-axes) and intergrown with hydrothermal quartz and carbonate phases (Fig. 5e). Crystals regularly display clear zonation in backscatter images (Fig. 5f), with darker cores and lighter rims. This may represent some shift in fluid chemistry during crystallisation, with the cores possibly crystallising at an earlier stage of ore formation. Syn-ore tourmaline is also present at P-64. Here hydrothermal tourmaline grains develop in haloes around auriferous veins, forming agglomerations of <10 μm , subhedral tourmaline crystals (Fig. 5g).

Replacive post-mineralization tourmaline is present only at Gara. Here, tourmaline replaces auriferous pyrite within the matrix of tourmalinite units (Fig. 5h), forming convex grain boundaries with pyrite crystals. This paragenetic stage has not been confirmed in any of the other deposits studied here. It should be stressed that Gara is the only deposit to display the complete tourmaline paragenesis, and for this reason has been the main focus of this study.

5. Samples and analytical methods

5.1. Sample descriptions

Three samples were analysed from the Gara deposit (LD44, LD27 and PT7). These were chosen as they contain representative tourmaline grains from all three paragenetic stages identified at Gara, including pre-mineralization sedimentary matrix replacement (LD44 and PT7), syn-ore needles in auriferous ankerite-quartz-pyrite veins (LD44) and post-ore tourmaline, replacing auriferous pyrite (LD44 and LD27). LD27 contains dominantly replacive tourmaline; however some grains likely represent earlier paragenetic stages (matrix replacement). All three samples contain significant concentrations of Au (7.5 to 27.8 g/t). One sample was analysed from Yalea North (YD82), with a Au grade of 2.5 g/t. This sample is representative of the mineralised hydrothermal breccia at Yalea North, containing euohedral to subhedral acicular hydrothermal tourmaline crystals interpreted to have grown syn-mineralization. This sample also contains clasts of early matrix replacement tourmaline, and rare multi-generation grains with anhedral cores and euohedral overgrowths. The latter likely represent older (pre-ore) tourmalines on which a hydrothermal overgrowth nucleated during ore formation. A single sample from P-64 (PT10) contains tourmaline associated with alteration haloes around veins, which are interpreted to be syn-mineralization. Tourmaline in this sample is cryptocrystalline (generally <50 μm). A single sample from the Baqata target area (BP1204)

contains cryptocrystalline tourmaline replacing the sedimentary matrix prior to ore formation. This sample has a Au grade of 8.4 g/t. In addition, two samples of granitic pegmatite from the Gamaye pluton (MOU03 and MOU04) were analysed to provide $\delta^{11}\text{B}$ values for local felsic magmatism. These contain coarse (up to 5 mm) tourmaline grains which show distinct colour zoning in plain polarized light.

5.2. Energy-dispersive X-ray spectroscopy

Major and trace-element mineral compositions were determined using an Oxford Instruments X-ACT energy-dispersive X-ray detector (EDS) mounted on a Zeiss EVO 50 Scanning Electron Microscope (SEM) at Kingston University London. EDS operation employed an accelerating voltage of 20 kV, a beam current of 1.5 na, and a detector process time of 4. Data collection and reduction was conducted using the Oxford Instruments INCA analytical suite. The detection limit for all elements was approximately 0.20 wt %.

5.3. Secondary Ion Mass Spectrometry

The Cameca 1280-HR instrument at the Helmholtz Zentrum Potsdam was used to conduct $\delta^{11}\text{B}$ determinations on tourmaline crystals from 9 samples collected from the study area. Samples were prepared as 25 mm diameter, round thin section mounts from which selected tourmaline grains were initially investigated by electron microprobe. Prior to SIMS analysis the samples were cleaned in an ultrasonic bath using high-purity ethanol, and then argon sputter coated with 35 nm of high-purity gold.

SIMS analyses employed a 400 pA, $^{16}\text{O}^-$ primary ion beam with a total energy of 23 keV, resulting in a beam diameter of *circa* 5 μm at the sample surface. Positive secondary ions were extracted using a +10 kV potential applied to the sample holder, to which no offset voltage was applied, in conjunction with a 50 eV wide energy window which was manually centred at the beginning of an analytical session to be *circa* 10 eV from the low energy flank of the secondary ion beam. Each analysis was preceded with a 2 nA, 90 second pre-sputtering of the target domain, with magnetic cycling performed throughout. Subsequently, the secondary beam was automatically centred on the field aperture, followed by the contrast aperture and, finally, the secondary magnetic field was re-centred using the $^{11}\text{B}^+$ mass station.

The $\delta^{11}\text{B}$ data was collected using mono-collection mode. A single analysis consisted of 50 cycles of the peak stepping sequence $^{10}\text{B}^+$ (4 s integration time per cycle) followed by $^{11}\text{B}^+$ (2 s integration time). The mass

resolution was set at $M/\Delta M \approx 2000$, which is effectively full transmission for the 1280-HR instrument; this provided more than adequate resolution to separate $^{11}\text{B}^+$ from $^{10}\text{B}^1\text{H}^+$. The typical count rate for $^{11}\text{B}^+$ under these conditions was *circa* 300,000 cps, to which a 46.2 ns dead time correction was applied, as defined by a delay line in the electron multipliers pre-amplifier circuitry. The total data collection time for a single point was 460 seconds.

Machine calibration made use of three reference materials: Harvard 112566 schorl, Harvard 108796 dravite and IAEA B4 tourmaline (Dyar et al., 2001; Gonfiantini et al., 2003; Tonarini et al., 2003; Leeman and Toranini, 2001). Overall analytical repeatability on individual RMs were around ± 0.53 , 0.63 and 0.93 ‰ (1 sd) for the schorl (N=20), dravite (N=17) and B4 (N=17). The observed variability for the instrument induced mass fractionation was around ± 0.93 ‰ (1 sd) when the results from all three RMs were pooled. Including additional sources of analytical uncertainty (e.g. uncertainty in the wet chemical results for the individual RMs, within-run uncertainties of the order ± 0.4 to ± 0.9 ‰, and the presence of any matrix effects impacting the schorl-dravite range of tourmaline chemistry) we estimate the overall reliability of our method to around ± 1.2 ‰ (1 sd).

6. Chemical compositions of tourmaline

The structural formulae of tourmalines from the SMSZ were calculated using the WinClastour program of Yavuz et al. (2006). The unit formulae were normalised to 15 cations (T + Z + Y). Tourmalines from the pegmatite dykes in the Gamaye pluton fall within the Li-poor (0.10 – 0.17 apfu; calculated) granite and pegmatite field (schorl) (Fig. 6). They are relatively Al-rich (6.4 to 6.6 apfu) and display high Fe/(Fe+Mg) ratios (0.72 – 0.95).

Hydrothermal tourmalines are readily distinguished from pegmatitic tourmalines by lower Fe/(Fe+Mg) ratios (0.04-0.73) and variable Al content (4.6 to 6.5 apfu) typically associated with metasedimentary rocks (metapelites, metapsammities and metacarbonates) (Fig. 6; Table 1). Tourmaline at Baqata and P-64 are more dravitic, whereas those at Gara and Yalea are characterized by intermediate compositions. The majority of hydrothermal tourmaline in the Loulo District is located close to the join between oxy-dravite and povondraite (Fig. 6). This trend is common in tourmalines from ore deposits that have formed from high salinity fluids and has been observed in tourmalines within meta-evaporite units (Henry et al., 2008).

All hydrothermal tourmalines belong to the alkali-group (Fig. 6). Vacancies in the X-site (X_{\square}) of hydrothermal tourmalines appear to vary systematically with paragenesis. Early grains at Gara, Baqata and Yalea North show X_{\square} from 0 to 0.24. X_{\square} in syn-mineralization and late stage grains ranges from 0.12 to 0.38 apfu. X-sites in paragenetically early grains show variation in both Ca (0 to 0.13 apfu) and Na (0.71 to 0.96 apfu). Ca content is lower and more frequently absent in later paragenetic stages, with a more restricted range (0 to 0.07 apfu). Na content in later tourmalines is generally lower than in early grains (0.62 to 0.88 apfu).

7. Boron isotope compositions of tourmaline

B-isotope data is listed in full in Table 2. The total range of B-isotope values in the Loulo-Bambadji District ($\delta^{11}\text{B} = -18.7$ to 19.8 ‰) shows a strongly bimodal first order distribution (Fig. 7). Tourmaline from the Gamaye pluton provides a control on $\delta^{11}\text{B}$ values of local magmatic-sourced boron. Data from two samples of pegmatite hosted tourmaline display a normal distribution with a mean of -17.1 ± 1.2 ‰ ($n=29$). A single detrital tourmaline grain hosted in the wall rock at Gara showed a similar $\delta^{11}\text{B}$ value of -15.5 ‰ ($n=2$).

Hydrothermal tourmaline associated with Au mineralization is characterised by heavier $\delta^{11}\text{B}$ values, ranging from -3.5 to $+19.8$ ‰ ($n=55$). Fig. 6 shows three $\delta^{11}\text{B}$ peaks within the hydrothermal tourmaline dataset. The main peak occurs at 14 ‰, with two minor peaks at 0 and 8 ‰.

The $\delta^{11}\text{B}$ of tourmaline at Gara ranges from -0.3 to 16.7 ‰ ($n=29$). The tourmaline paragenesis at Gara is very clear and allows examination of changes in $\delta^{11}\text{B}$ from pre-ore alteration to post-ore replacement. Fig. 8a shows that pre-ore tourmaline in altered quartz wacke matrix displays heavy $\delta^{11}\text{B}$ values, between 8 and 16.7 ‰ (mean of 12.7 ‰; $n=12$). By contrast; syn-ore tourmaline needles ($n=3$) and replacive crystals ($n=14$) show a lighter range of $\delta^{11}\text{B}$ values (-0.3 to 15.1 ‰) (Fig. 8b and c), with identical means of ~ 5 ‰. This suggests that syn-ore and post-ore tourmalines are isotopically indistinguishable. Furthermore, the distribution of the B-isotope data for early tourmalines and syn- to –late ore tourmalines show a negative and positive skew, respectively.

Early clast bound tourmalines and inherited tourmaline crystal clasts in the Yalea North hydrothermal breccia yielded $\delta^{11}\text{B}$ values between 12.2 and 19.8 ‰ ($n=4$). Cores of hydrothermal tourmalines from the breccia yielded $\delta^{11}\text{B}$ from 6.6 to 9.3 ‰ ($n=3$); a single rim analysis gave a value of -0.5 ‰. Paragenetically

early, matrix bound tourmaline at the Baqata target is homogenous, with a range from 13 to 15.9 ‰ (mean of 14 ‰; $n=9$). P-64 exhibits the lightest $\delta^{11}\text{B}$ values for hydrothermal tourmaline in the region, with a mean of 0.1 ‰ ($n=9$); values range from -3.5 up to 9.6 ‰.

Heavy $\delta^{11}\text{B}$ in hydrothermal tourmalines in the Loulo district correlates to high X-site Na ($r=0.416$), Ca ($r=0.677$), and total X-occupancy ($r=0.688$) (Fig. 9). Furthermore, $\delta^{11}\text{B}$ and X-site occupancy vary with paragenesis, with pre-ore tourmalines exhibiting higher $\delta^{11}\text{B}$ and X-site occupancy than syn-mineralisation and replacive grains.

8. Discussion

8.1. Discriminating multiple fluid sources in the Loulo Mining District

The $\delta^{11}\text{B}$ data from hydrothermal tourmaline in the Loulo Mining District (-3.5 to 19.8 ‰; $n=55$) falls broadly within the fields of B in tourmaline hosted in clastic metasediments, marbles and marine meta-evaporites (van Hinsberg et al., 2011b; Marschall and Jiang, 2011 and references therein; Fig. 7). In contrast, the $\delta^{11}\text{B}$ data from tourmaline in the Gamaye pluton (mean of -17.1 ‰; $n=29$) fall at the light end of the global granite and pegmatite field, and within the field typical of tourmaline hosted in granite related vein systems worldwide (Jiang and Palmer, 1998). This distribution excludes the presence of a magmatic-sourced B component in the hydrothermal ore bodies of the LBD and suggests a metamorphic source for both B-bearing hydrothermal fluids.

In detail, the $\delta^{11}\text{B}$ data from the paragenetically resolved tourmalines at the Gara deposit provide clear evidence of a shift in fluid source from pre- to post-mineralisation. Figure 8a shows that early stage tourmalines (pre-mineralization) are characterised by heavy $\delta^{11}\text{B}$, with a primary peak at 12 ‰ and a secondary peak at 16 ‰. These data fall comfortably within the range of tourmalines hosted in marine meta-evaporites. The $\Delta^{11}\text{B}_{\text{tourmaline-fluid}}$ at 300°C (estimated temperature of mineralization at Gara; Lawrence et al., 2013b) is -3.7 ‰ (using the equation of Meyer et al., 2008); therefore the $\delta^{11}\text{B}$ of the fluid from which tourmaline precipitated would have been 11.7 to 19.7 ‰. This places the main peak at $\delta^{11}\text{B}$ values just below the marine evaporite field and the secondary peak within the field. Syn-mineralization (Fig. 8b) and post-mineralization replacement tourmaline (Fig. 8c) at Gara display lighter $\delta^{11}\text{B}$ values, from -0.3 to 15.1. These $\delta^{11}\text{B}$ values are indicative of fluids sourced from marine carbonates and metasediments, with some

minor overlap with the lighter end of the field for tourmalines in meta-evaporites (Fig. 7). Such a source is consistent with the lithological characteristics of the Kofi Series (Lawrence et al., 2013a). A similar pattern is repeated in the wider dataset. Fig. 7 shows that the $\delta^{11}\text{B}$ peak at 14 ‰ is dominated by pre-mineralization tourmaline from Gara and Baqata and from Yalea North. The calculated $\delta^{11}\text{B}_{\text{fluid}}$ value for this peak sits within analytical error (1.2 ‰) of the marine evaporite field. Conversely, the peak at 0 ‰ is largely controlled by $\delta^{11}\text{B}$ values from syn-mineralization tourmaline at P-64 and Gara deposits. This suggests that the main stage of mineralization at these deposits, as well as the replacement stage at Gara, was dominated by fluids sourced from devolatilisation of marine carbonates and/or clastic metasediments. The spread of the data to $\delta^{11}\text{B}_{\text{fluid}}$ values up to 15.1 ‰ may represent some influence from heavier, evaporite sourced ratios as a result of the fluid mixing described by Lawrence et al. (2013b). Indeed, it seems likely that the range and skewed distribution of $\delta^{11}\text{B}$ in early tourmaline and the late and syn-ore tourmaline represents a process of continuous tourmaline growth throughout the process of fluid mixing and mineralisation.

Tourmaline X-site occupancy (variable Na \pm Ca) correlates with $\delta^{11}\text{B}$ ($r=0.688$; Fig. 9). X-site occupancy has been suggested by von Goerne et al. (2011) to be indicative of fluid compositions. Evaporites contain very high proportions of carbonate, sulphate, and halide minerals over km-scale thicknesses (Land et al., 1995). Evaporite units can also be major reservoirs for boron, with concentrations of up to 9000 ppm (Dutrow and Henry, 2011), much of which would become mobilised along with Ca and Na (through breakdown of gypsum and halite) during regional metamorphism (c.f. McKibben et al. 1988). Marine carbonates and clastic metasediments also represents a viable source for B in hydrothermal fluids, with concentrations of up to 250 ppm recorded in metapelites (Dutrow and Henry, 2011) and up to 71 ppm in marine carbonates (Hemming and Hanson, 1992). The correlation of high X-site occupancy and $\delta^{11}\text{B}$ in pre-ore tourmalines in the LBD indicate precipitation from a hypersaline fluid with high concentrations of Na and Ca, derived from a meta-evaporite source. Later tourmalines, which show lower $\delta^{11}\text{B}$ and X-site occupancy (indicating a common fluid source for both stages), were sourced from carbonates and clastic metasediments and contained lower amounts of Ca and Na. A source of hydrothermal fluids within the host metasedimentary sequence in the LBD suggests that Au is also likely sourced from within the same sequence, as suggested by Lambert-Smith et al. (2016b). This sequential shift from evaporate derived brines to metasediment derived fluids makes sense in the context of metamorphic devolatilisation reactions, as minerals such as gypsum,

anhydrite, and halite would break down at lower P-T than clay minerals and phyllosilicates.

8.2. Evaporites in the Kofi Series?

There is no direct field evidence of evaporite units in the Kofi Series (Lawrence et al., 2013a; Lawrence et al., 2013b; Lambert-Smith et al., 2016a). Nevertheless, the age of the host rocks, their geological setting and isotopic characteristics appear to support our interpretation. The period from 2.22 to 2.06 Ga is characterised by a global positive $\delta^{13}\text{C}$ excursion, which coincides with world-wide deposition of evaporites and red beds (Melezhik et al., 1999; Schroder et al., 2008). The youngest detrital zircon from the tourmalinite at Gara has a U-Pb age of 2093 ± 7 Ma (Boher et al., 1992), suggesting that deposition of the Kofi Series began during this time period. On a local scale, the presence of texturally immature siliciclastic and sandy marine carbonate rocks is consistent with a palaeoenvironment in which evaporites might have developed. This is further supported by isotopically heavy diagenetic ($\delta^{34}\text{S}$ from 19.7 to 25.4 ‰) and auriferous (11 to 15 ‰) pyrite from the Kofi Series (Lawrence et al., 2013b; Lambert-Smith et al., 2016b). ^{34}S becomes concentrated in sulphate phases in evaporite sequences (Ohmoto, 1986), and so heavy $\delta^{34}\text{S}$ values are consistent with the reduction of evaporite hosted sulphate minerals during diagenesis. Isotopically heavy auriferous pyrite in the LBD (11 to 15 ‰) tends to be associated with tourmalinized wall rock, whereas pyrite associated with other alteration facies (sericite-chlorite) is generally less ^{34}S -rich (0 to 12 ‰). Furthermore, a single paired δD and $\delta^{18}\text{O}$ analysis of tourmaline separates at Gara by Fouillac et al. (1993) indicated a marine contribution to hydrothermal waters. This was initially interpreted to indicate a marine exhalative setting for tourmaline growth; however, in light of our more extensive isotopic dataset it now lends further support to a marine evaporite fluid source.

Alternative explanations for this distribution of $\delta^{11}\text{B}$ values must be considered. The possibility that Rayleigh fractionation in a chemically closed system has affected the $\delta^{11}\text{B}$ values throughout the district seems unlikely. If this were the case, precipitation of tourmaline from a single initially homogenous fluid may, through continuous fractionation, eventually give rise to considerably heavier values of $\delta^{11}\text{B}$ in the residual fluid. We consider this not to be the case here as: 1) the data presented were collected from a large volume of rock, in which it is geologically unreasonable to assume closed system behaviour; 2) as shown for the Gara deposit, the B-isotope ratios become lighter through time, opposite to the expected effect of Rayleigh

fractionation on $\delta^{11}\text{B}$ in tourmaline (Marschall et al., 2009).

8.3. B-isotopic constraints on fluid mixing

These data can be placed into the context of the fluid mixing model proposed by Lawrence et al. (2013b).

The early timing of sodic alteration and the greater proportion of tourmalinization relative to mineralisation implies that the heavy $\delta^{11}\text{B}$, meta-evaporite derived fluid was widely circulating prior to main stage mineralization in the Loulo district. The dramatic shift to lighter isotopic ratios in syn- to post-mineralization tourmaline correlates with a distinct change in fluid chemistry, indicating a change in the fluid source (Fig. 7, 8 and 9).

Fig. 7b shows that, in addition to the light and heavy $\delta^{11}\text{B}$ peaks, a third peak is present at ~ 8 ‰, comprising data from all three paragenetic stages. This middle peak may represent a mixed isotopic signature arising directly from fluid mixing between the dilute aqueous-carbonic fluid and the high salinity fluid. If it is assumed that the peaks at 14 and 0 ‰ are representative of the end-member fluids in the Loulo region (hypersaline brine at 400 °C, 41.7 wt. % NaCl and aqueous-carbonic fluid at 275 °C, 6.1 wt. % NaCl, respectively), then a simple binary mixing model would indicate that the peak at 8 ‰ would result from an X_{brine} (fraction of brine end member) of 0.55 to 0.66. This, however, assumes equal concentrations of B in both end member fluids, which is highly unlikely. The absolute concentrations of B in the end-member fluids are unknown; however we may estimate the mixing ratio of these two fluids by using geologically reasonable estimates of their contained B. Garofalo et al. (2015) reported a mean B concentration in fluid inclusions from five separate orogenic gold deposits of 610 $\mu\text{g/g}$. Dutrow and Henry (2011) report maximum B concentrations in brines of 2160 ppm. These concentrations were assigned to the aqueous-carbonic fluid and the brine, respectively, and then integrated into the fluid mixing model, using the following equation (after Schwin et al., 2006):

$$\delta^{11}\text{B}_M = \left(\frac{m_B f_B}{m_B f_B + m_{AC}(1 - f_B)} \right) \cdot \delta^{11}\text{B}_B + \left(\frac{m_{AC}(1 - f_B)}{m_B f_B + m_{AC}(1 - f_B)} \right) \cdot \delta^{11}\text{B}_{AC}$$

Where $\delta^{11}\text{B}_B$, $\delta^{11}\text{B}_{AC}$, and $\delta^{11}\text{B}_M$ represent B-isotope values for the brine, the aqueous-carbonic fluid, and the mixture, respectively; m_B and m_{AC} are the molalities of B in the brine and aqueous-carbonic fluid, respectively. An X_{brine} of 0.25 produces a $\delta^{11}\text{B}$ of 7.8 ‰, suggesting that the brine was volumetrically

subordinate during ore formation. Calculated $\delta^{11}\text{B}_{\text{fluid}}$ for this mixing ratio indicates a mixture of heavy marine evaporite sourced B and lighter carbonate and terrigenous marine sediment sourced B (Fig. 10). The peak at 0 ‰ represents the eventual shift to the metasedimentary fluid source during the course of ore formation.

8.4. Implications for fluid and metal sources in orogenic gold deposits

The fluid sources discussed here support existing models for the source of Au in orogenic systems. The $\delta^{11}\text{B}$ data from syn-mineralization tourmaline in the Loulo district indicate a dominant fluid contribution from clastic metasediments and carbonate rocks. This suggests that metamorphic devolatilisation in the host terrane as the most likely process that gave rise to the ore forming fluids (c.f. Phillips and Powell, 2010; Tomkins, 2010; Pitcairn et al., 2014a & b). The Loulo Mining district represents something of an unusual case in orogenic deposits due to the remarkably high abundance of tourmaline. Indeed, tourmalinites *sensu stricto* (stratiform) are more commonly associated with VMS deposits (Palmer and Slack, 1989).

Nevertheless, we have demonstrated that B-isotopes in tourmaline can be instrumental in understanding a highly complex and dynamic hydrothermal system and identifying at least two isotopically distinct fluid sources.

Garofalo et al. (2014) conducted LA-ICP-MS analysis of fluid inclusions from five separate orogenic gold deposits, each with differing age, host rock lithology and mineral assemblage. The chemistry and microthermometric behaviour of these fluids was uniform and consistent with the commonly described orogenic ore fluid (Goldfarb et al., 2005): dilute (<6.5 wt. % NaCl equiv.) aqueous-carbonic fluids $\pm\text{CH}_4\pm\text{N}_2$ that homogenise between 200 and 400°C; similar to the aqueous-carbonic ore fluid at Loulo). However, Garofalo et al. (2014) also reported that fluids from all 5 deposits were consistently enriched in Au, B, As and Sb above lower crustal values, with B the third most abundant element in solution (up to 2200 $\mu\text{g/g}$), after Na and K. This common occurrence of B as an integral constituent of orogenic ore forming fluids, is reflected in the presence of tourmaline as a common gangue mineral in orogenic gold systems globally and across time (e.g. Olivo et al., 2002; Batemen and Bierlein, 2007; Vial et al., 2007; Krienitz et al., 2008; Mao et al., 2008; Klein and Fuzikawa, 2010; Bark and Weihed, 2012; Kouhestani et al., 2014; Klein et al., 2015). Indeed, such wide distribution of a robust recorder of isotopic processes and fluid properties offers an

excellent opportunity to compare the fluid evolution and fluid and metal sources across a large proportion of deposits in the orogenic gold class. While there are alternate isotope systems which offer opportunity for cross comparison (O, C, S), these are largely restricted to minerals whose isotopic record may be overprinted during protracted ore formation processes (e.g. reequilibration of $\delta^{18}\text{O}$ values in quartz and carbonate minerals).

Currently, the $\delta^{11}\text{B}$ database for orogenic gold deposits is rather limited (Fig. 11); nevertheless, the range of the data is considerable (-24.1 to +19.8 ‰). Despite this variation, ore forming fluids are largely interpreted to result from metamorphic devolatilisation (Jiang et al., 2002; Krientiz et al., 2008; Beaudoin et al., 2013; Molnar et al., 2016), with some influence from fluid mixing (Krientiz et al., 2008). We suggest that this variability tentatively demonstrates that specific source rocks are not necessarily critical in generating an auriferous 'orogenic gold fluid'. This is not to say that the specific geology of individual deposits and their host terranes is not important; clearly geological heterogeneities can play a key role to in ore formation, such as in the Loulo District. However, regardless of these 'local' effects, we still see the consistent development of orogenic gold deposits from a common ore fluid, in reoccurring tectonic settings. This suggests that examination of the wider geo-dynamic settings may be more important in understanding ore genesis. Fittingly, Wyman et al. (2016) have recently articulated the need to adopt a mineral systems approach in furthering our understanding of the orogenic gold class.

9. Conclusions

We have demonstrated that B-isotopes in hydrothermal tourmaline, when analysed in situ and compared to mineral chemistry and fluid inclusion analyses, have tremendous potential to resolve complex hydrothermal systems with multiple fluid sources.

The orogenic gold deposits in the Loulo Mining District show a significant isotopic shift from heavy $\delta^{11}\text{B}$ values in pre-mineralization tourmaline to lighter values in syn-mineralization and late replacement phases. This is interpreted to represent a shift from a hypersaline fluid arising from evaporate breakdown during prograde metamorphism, responsible for widespread pre-ore Na- and B-metasomatism, to an aqueous-carbonic dominated system with mixing of the two fluids during ore formation. The $\delta^{11}\text{B}$ values of the dominant aqueous-carbonic fluid suggest derivation from devolatilisation of clastic marine metasediments

and carbonate rocks.

This paper does not wish to suggest that all orogenic gold deposits are sourced from devolatilisation of sedimentary rocks during metamorphism. However we do demonstrate that $\delta^{11}\text{B}$ analysis can provide a robust means of testing the level of source region variability in orogenic gold fluids, and by extension, the variability in metal sources. This may be achieved through the application of B-isotope analysis across the spectrum of orogenic gold deposits, many of which are sufficiently enriched in B to feature tourmaline as a gangue phase. Whether or not this yields unequivocal evidence in support of a common source for orogenic gold, such a comparison would no doubt improve our understanding of this complex deposit class.

Acknowledgements

This research was funded by Randgold Resources and the SIMS laboratory at the Helmholtz Centre, Potsdam. We would like to express our gratitude to Paul Harbidge, Reinet Harbidge and Joel Holliday (Randgold Resources) for their input, advice and collaboration. Frédéric Couffignal (SIMS laboratory, Helmholtz Centre, Potsdam), Richard Giddens, and Ian Gill (Kingston University London) are acknowledged for their technical contributions. The authors also wish to thank Gawen Jenkin for useful discussions in the early stages of preparing this manuscript. Lastly we wish to thank the two anonymous reviewers for their constructive comments that have significantly improved the manuscript.

References

Allibone A., Teasdale J., Cameron G., Etheridge M., Uttley P., Soboh A., Appiah-Kubi J., Adanu A., Arthur R., Mamphey J., Odoom B., Zuta J., Tsikata A., Pataye F. and Famiyeh S. (2002) Timing and structural controls on gold mineralization at the Bogoso gold mine, Ghana, West Africa. *Econ Geol*, **97**, 949-969.

Bark G. and Weihed P. (2012) Geodynamic settings for Paleoproterozoic gold mineralization in the Svecofennian domain: A tectonic model for the Fäboliden orogenic gold deposit, northern Sweden. *Ore Geol Rev*, **48**, 403-412.

Bassot J.P. and Caen-Vachette M. (1984) Données géochronologiques et géochimiques nouvelles sur les granitoides de l'Est du Sénégal: implications sur l'histoire géologique du Birrimien de cette région. In *African Geology* (eds. J. Klerkx and J. Michot). Tervuren, Belgium, 196-209.

Bateman R. and Bierlein F. P. (2007) On Kalgoorlie (Australia), Timmins–Porcupine (Canada), and factors in intense gold mineralization. *Ore Geol Rev*, **32**, 187-206.

Beaudoin G. and Pitre D. (2005) Stable isotope geochemistry of the Archean Val-d 'Or (Canada) orogenic gold vein field. *Miner Deposita*, **40**, 59-75.

Beaudoin G., Rollion-Bard C., Giuliani G. (2013) The boron isotope composition of tourmaline from the Val-d'Or orogenic gold deposits, Québec, Canada. *Proceedings of the 19th Biennial SGA Meeting, Uppsala*, 3, 1090–1092.

Bierlein F.P. and McKnight S. (2005) Possible intrusion-related gold systems in the western Lachlan Orogen, southeast Australia. *Econ Geol*, **100**, 385-398.

Boher M., Abouchami W., Michard A., Albarede F. and Arndt N.T. (1992) Crustal growth in West Africa at 2.1 Ga. *J Geophys Res*, **97**, 345-369.

Davis D.W., Hirdes W., Schaltegger U. and Nunoo E.A. (1994) U-Pb age constraints on deposition and provenance of Birimian and gold-bearing Tarkwaian sediments in Ghana, West Africa. *Precambrian Res*, **67**, 89-107.

De Kock G.S., Armstrong R.A., Siegfried H.P. and Thomas E. (2011) Geochronology of the Birim Supergroup of the West African craton in the Wa-Bolé region of west-central Ghana: Implications for the stratigraphic framework. *J Afr Earth Sci*, **59**, 1-40.

Dia A., Van Schmus W.R. and Kröner A. (1997) Isotopic constraints on the age and formation of a Palaeoproterozoic volcanic arc complex in the Kédougou inlier, eastern Senegal, West Africa. *J Afr Earth Sci*, **24**, 197-213.

Dommanget A., Milési J.P. and Diallo M. (1993). The Loulo gold and tourmaline-bearing deposit. *Mineralium Deposita*, **28**, 253-263.

Duncan R.J., Buick I.S., Kobayashi K. and Wilde A.R. (2014) Chemical and stable isotopic characteristics of syn-tectonic tourmaline from the Western fold belt, Mount Isa inlier, Queensland, Australia. *Chem Geol*, **381**, 131-143.

Dutrow B.L. and Henry D.J. (2011) Tourmaline: a geologic DVD. *Elements*, **7**, 301-306.

Dyar M.D., Wiedenbeck M., Robertson D., Cross L.R., Delaney J.S., Ferguson K., Francis C.A., Grew E.S., Guidotti C.V., Hervig R.L., Hughes J.M., Husler J., Leeman W., McGuire A.V., Rhede D., Rothe H., Paul R.L., Richards I. and Yates M. (2001) Reference minerals for microanalysis of light elements. *Geostandard Newslett*, **25**, 441–463.

Feybesse J., Billa M., Guerrot C., Duguey E., Lescuyer J., Milési J.P. and Bouchot V. (2006) The Palaeoproterozoic Ghanaian province: Geodynamic model and ore controls, including regional stress modelling. *Precambrian Res*, **149**, 149-196.

Fouillac A.M., Dommaget A., and Milési J.P. (1993) A carbon, oxygen, hydrogen and sulfur isotopic study of the gold mineralization at Loulo, Mali. *Chem Geol*, **106**, 47–62.

Gaboury D. (2013) Does gold in orogenic deposits come from pyrite in deeply buried carbon-rich sediments? Insight from volatiles in fluid inclusions. *Geology*, **41**, 1207–1210.

Garda G. M., Trumbull R. B., Beljavskis P., and Wiedenbeck M. (2009) Boron isotope composition of tourmalinite and vein tourmalines associated with gold mineralization, Serra do Itaberaba Group, central Ribeira Belt, SE Brazil. *Chem Geol*, **264**, 207-220.

Garofalo P.S., Fricker M.B., Günther D., Bersani D., and Lottici P.P. (2014) Physical-chemical properties and metal budget of Au-transporting hydrothermal fluids in orogenic deposits. In Garofalo P. S. and Ridley J. R. (eds.) *Gold-Transporting Hydrothermal Fluids in the Earth's Crust*. Geological Society, London, Special Publications, **402**, 71-102.

von Goerne, G., Franz, G. and van Hinsberg, V.J. (2011). Experimental determination of Na–Ca distribution between tourmaline and fluid in the system $\text{CaO–Na}_2\text{O–MgO–Al}_2\text{O}_3\text{–SiO}_2\text{–B}_2\text{O}_3\text{–H}_2\text{O}$. *The Canadian Mineralogist*, **49**, 137-152.

Goldfarb R.J., Newberry R.J., Pickthorn W.J. and Gent C.A. (1991) Oxygen, hydrogen, and sulphur isotope studies in the Juneau Gold Belt, Southeastern Alaska: constraints on the origin of hydrothermal fluids. *Econ Geol*, **86**, 66-80.

Goldfarb R.J., Baker T., Dubé B., Groves D.I., Hart C.J.R. and Gosselin P. (2005) Distribution, character, and genesis of gold deposits in metamorphic terranes. *Econ Geol*, **100th anniversary volume**, 407–450.

Gonfiantini R., Tonarini S., Gröning M., Adorni-Braccesi A., Al-Ammar A. S., Astner M., Bächler S., Barnes R. M., Bassett R. L., Cocherie A., Deyhle A., Dini A., Ferrara G., Gaillardet J., Grimm J., Guerrot C., Krähenbühl U., Layne G., Lemarchand D., Meixner A., Northington D. J., Pennisi M., Reitznerová E., Rodushkin I., Sugiura N., Surberg R., Tonn S., Wiedenbeck M., Wunderli S., Xiao Y. and Zack T. (2003) Intercomparison of boron isotope and concentration measurements. Part II: evaluation of results. *Geostandard Newslett*, **27**, 41–57

Groves D.I., Goldfarb R.J., Gebre-Mariam M., Hagemann S.G. and Robert F. (1998) Orogenic gold deposits: A proposed classification in the context of their crustal distribution and relationship to other gold deposit types. *Ore Geol Rev*, **13**, 7-27.

Gueye M., Siegesmund S., Wemmer K., Pawlig S., Drobe M., Nolte N. and Layer P. (2007) New evidence for an early Birimian evolution in the West African Craton: an example from the Kédougou-Kéniéba inlier, southeast Senegal. *S Afr J Geol*, **110**, 511-534.

Hedenquist J.W. and Lowenstern J.B. (1994) The role of magmas in the formation of hydrothermal ore deposits. *Nature*, **370**, 519-527.

Hemming N.G. and Hanson G.N. (1992) Boron isotopic composition and concentration in modern marine carbonates. *Geochim Cosmochim Acta*, **56**, 537-543.

Henry D.J. and Guidotti C.V. (1985) Tourmaline as a petrogenetic indicator mineral- an example from the staurolite-grade metapelites of NW Maine. *Am Mineral*, **70**, 1-15.

Henry D.J., Sun H., Slack J.F., and Dutrow B.L. (2008) Tourmaline in meta-evaporites and highly magnesian rocks: perspectives from Namibian tourmalinites. *Eur J Mineral*, **20**, 889-904.

Hirdes W., Davis D.W. and Eisenlohr B.N. (1992) Reassessment of Proterozoic granitoid ages in Ghana on the basis of U/Pb zircon and monazite dating. *Precambrian Res*, **56**, 89-96.

Hirdes W. and Davis D.W. (2002) U-Pb Geochronology of Palaeoproterozoic rocks in the southern part of the Kédougou-Kéniéba inlier, Senegal, West Africa: evidence for diachronous accretionary development of the Eburnean Province. *Precambrian Res*, **118**, 83-99.

Hronsky J.M., Groves D.I., Loucks R.R., and Begg G.C. (2012) A unified model for gold mineralization in accretionary orogens and implications for regional-scale exploration targeting methods. *Miner Deposita*, **47**, 339-358.

Jiang, S.Y. and Palmer, M.R., 1998. Boron isotope systematics of tourmaline from granites and pegmatites; a synthesis. *European Journal of Mineralogy*, **10**, 1253-1265.

Jiang S.Y., Palmer M.R., and Yeats C.J. (2002) Chemical and boron isotopic compositions of tourmaline from the Archean Big Bell and Mount Gibson gold deposits, Murchison Province, Yilgarn Craton, Western Australia. *Chem Geol*, **188**, 229-247.

John T., Klemd R., Hirdes W. and Loh G. (1999) The metamorphic evolution of the Palaeoproterozoic (Birimian) volcanic Ashanti belt (Ghana, West Africa). *Precambrian Res*, **98**, 11-30.

Kerrick R. and Wyman D. (1990) Geodynamic setting of mesothermal gold deposits: An association with accretionary tectonic regimes. *Geology*, **18**, 882-885.

Kouhestani H., Rashidnejad-Omran N., Rastad E., Mohajjel M., Goldfarb R.J., and Ghaderi M. (2014) Orogenic gold mineralization at the Chah Bagh deposit, Muteh gold district, Iran. *J Asian Earth Sci*, **91**, 89-106.

Klein E. L., and Fuzikawa K. (2010) Origin of the CO₂-only fluid inclusions in the Palaeoproterozoic Carará vein-quartz gold deposit, Ipitinga Auriferous District, SE-Guiana Shield, Brazil: Implications for orogenic gold mineralization. *Ore Geol Rev*, **37**, 31-40.

Klein E.L., Lucas F.R., Queiroz J.D., Freitas S.C., Renac C., Galarza M.A., Jourdan F. and Armstrong R. (2015) Metallogenesis of the Paleoproterozoic Piaba orogenic gold deposit, São Luís cratonic fragment, Brazil. *Ore Geol Rev*, **65**, 1-25.

Krienitz M.S., Trumbull R.B., Hellmann A., Kolb J., Meyer F.M., and Wiedenbeck M. (2008)

Hydrothermal gold mineralization at the Hira Buddini gold mine, India: constraints on fluid evolution and fluid sources from boron isotopic compositions of tourmaline. *Miner Deposita*, **43**, 421-434. Lambert-Smith, J.S., Lawrence, D.M., Müller, W. and Treloar, P.J., 2016a. Palaeotectonic setting of the south-eastern Kédougou-Kéniéba Inlier, West Africa: new insights from igneous trace element geochemistry and U-Pb zircon ages. *Precambrian Research*, **274**, 110-135. doi:10.1016/j.precamres.2015.10.013.

Lambert-Smith, J.S., Lawrence, D.M., Vargas, C.A., Boyce, A.J., Treloar, P.J. and Herbert, S., 2016b. The Goukoto Au deposit, West Africa: Constraints on ore genesis and volatile sources from petrological, fluid inclusion and stable isotope data. *Ore Geology Reviews*, **78**, 606-622 doi:10.1016/j.oregeorev.2015.10.025.

Land L.S., Eustice R.A., Mack L.E., and Horita J. (1995) Reactivity of evaporites during burial: An example from the Jurassic of Alabama. *Geochim Cosmochim Acta*, **59**, 3765-3778.

Large R.R., Bull S.W. and Maslennikov V.V. (2011) A carbonaceous sedimentary source-rock model for Carlin-type and orogenic gold deposits. *Econ Geol*, **106**, 331-358.

Lawrence D.M., Treloar P.J., Rankin A.H., Harbidge P. and Holliday J. (2013a) The Geology and Mineralogy of the Loulo Mining District, Mali, West Africa: Evidence for Two Distinct Styles of Orogenic Gold Mineralization. *Econ Geol*, **108**, 199-227.

Lawrence D.M., Treloar P.J., Rankin A.H., Boyce A. and Harbidge P. (2013b) A fluid inclusion and stable isotope study at the Loulo mining district, Mali, West Africa: Implications for multifluid sources in the generation of orogenic gold deposits. *Econ Geol*, **108**, 229–257.

Leeman W. and Tonarini S. (2001) Boron isotopic analysis of proposed borosilicate mineral reference samples. *Geostandard Newslett*, **25**, 399–403.

Mao J., Wang Y., Li H., Pirajno F., Zhang C. and Wang R. (2008) The relationship of mantle-derived fluids to gold metallogenesis in the Jiaodong Peninsula: evidence from D–O–C–S isotope systematics. *Ore Geol Rev*, **33**, 361-381.

Marschall H.R., Meyer C., Wunder B., Ludwig T. and Heinrich W. (2009) Experimental boron isotope

fractionation between tourmaline and fluid: confirmation from in situ analyses by secondary ion mass spectrometry and from Rayleigh fractionation modelling. *Contrib Mineral Petr*, **158**, 675-681.

Marschall, H.R. and Jiang, S.Y., 2011. Tourmaline isotopes: no element left behind. *Elements*, **7**, 313-319.

Masurel, Q., Thébaud, N., Miller, J., Ulrich, S. and Hein, K.A., 2015. The Alamoutala carbonate-hosted gold deposit in Mali, West Africa. *Ore Geology Reviews*. doi:10.1016/j.oregeorev.2015.10.012.

McCuaig T.C. and Kerrich R., (1998) P-T-t deformation-fluid-characteristics of lode gold deposits: Evidence from alteration systematics. *Ore Geol Rev*, **12**, 381-454.

McKibben M.A., Williams A.E. and Okubo S. (1988) Metamorphosed Plio-Pleistocene evaporites and the origins of hypersaline brines in the Salton Sea geothermal system, California: Fluid inclusion evidence. *Geochim Cosmochim Ac*, **52**, 1047-1056.

Melezhik V.A., Fallick A.E., Medvedev P.V. and Makarikhin V.V. (1999) Extreme $\delta^{13}\text{C}_{\text{carb}}$ enrichment in ca. 2.0 Ga magnesite–stromatolite–dolomite–red beds' association in a global context: a case for the world-wide signal enhanced by a local environment. *Earth-Sci Rev*, **48**, 71-120.

Meyer C., Wunder B., Meixner A., Romer R.L. and Heinrich W. (2008) Boron-isotope fractionation between tourmaline and fluid: an experimental re-investigation. *Contrib Mineral Petr*, **156**, 259-267.

Molnár F., Mänttari I., O'Brien H., Lahaye Y., Pakkanen L., Johanson B., Käpyaho A., Sorjonen-Ward P., Whitehouse M. and Sakellaris G. (2016). Boron, sulphur and copper isotope systematics in the orogenic gold deposits of the Archaean Hattu schist belt, eastern Finland. *Ore Geol Rev*, **77**, 133-162.

Oberthür T., Vetter U., Davis D.W. and Amanor J.A. (1998) Age constraints on gold mineralization and Palaeoproterozoic crustal evolution in the Ashanti belt of southern Ghana. *Precambrian Res*, **89**, 129-143.

Ohmoto H. (1986) Stable isotope geochemistry of ore deposits. In *Stable isotopes in high temperature geological processes* (eds. J.E. Valley, H.P. Taylor and J.R. O'Neil). *Rev Mineral*, **16**, 491-560.

Olivo G.R. and Williams-Jones A.E. (2002) Genesis of the auriferous C quartz-tourmaline vein of the

Siscoe mine, Val d'Or district, Abitibi subprovince, Canada: structural, mineralogical and fluid inclusion constraints. *Econ Geol*, **97**, 929-947.

Palmer M.R. and Slack J.F. (1989) Boron isotopic composition of tourmaline from massive sulfide deposits and tourmalinites. *Contrib Mineral Petr*, **103**, 434-451.

Perrouy S., Aillères L., Jessell M.W., Baratoux L., Bourassa Y. and Crawford B. (2012) Revised Eburnean geodynamic evolution of the gold-rich southern Ashanti Belt, Ghana, with new field and geophysical evidence of pre-Tarkwaian deformations. *Precambrian Res*, **204**, 12-39.

Phillips G.N. (1993) Metamorphic fluids and gold. *Mineralogical Magazine*, **57**, 365–374.

Phillips G.N. and Powell R. (2009) Formation of gold deposits: Review and evaluation of the continuum model. *Earth-Sci Rev*, **94**, 1-21.

Phillips G.N. and Powell R. (2010) Formation of gold deposits: a metamorphic devolatilization model. *J Metamorph Geol*, **28**, 689-718.

Powell R., Will T.M. and Phillips G.N. (1991) Metamorphism in Archaean greenstone belts: calculated fluid compositions and implications for gold mineralization. *J Metamorph Geol*, **9**, 141-150.

Pitcairn I.K., Craw D. and Teagle D.A. (2014a) Metabasalts as sources of metals in orogenic gold deposits. *Miner Deposita*, **50**, 1-18.

Pitcairn, I.K., Craw, D. and Teagle, D.A. (2014b) The gold conveyor belt: Large-scale gold mobility in an active orogen. *Ore Geology Reviews*, **62**, 129-142.

Schröder S., Bekker A., Beukes N.J., Strauss H. and Van Niekerk H.S. (2008) Rise in seawater sulphate concentration associated with the Paleoproterozoic positive carbon isotope excursion: evidence from sulphate evaporites in the ~ 2.2–2.1 Gyr shallow-marine Lucknow Formation, South Africa. *Terra Nova*, **20**, 108-117.

Schwartz M.O. and Melcher F. (2004) The Falémé Iron District, Senegal. *Econ Geol*, **99**, 917-939.

Schwinn, G., Wagner, T., Baatartsogt, B. and Markl, G., 2006. Quantification of mixing processes in

ore-forming hydrothermal systems by combination of stable isotope and fluid inclusion analyses. *Geochim Cosmochim Acta*, **70**, 965-982.

Slack J. F. and Trumbull R. B. (2011) Tourmaline as a recorder of ore-forming processes. *Elements*, **7**, 321-326.

Taylor P.N., Moorbath S., Leube A. and Hirdes W. (1992) Early Proterozoic crustal evolution in the Birimian of Ghana: constraints from geochronology and isotope geochemistry. *Precambrian Res*, **56**, 97-111.

Tomkins A.G. (2010) Windows of metamorphic sulfur liberation in the crust: Implications for gold deposit genesis. *Geochim Cosmochim Acta*, **74**, 3246-3259.

Tomkins A.G. (2013) On the source of orogenic gold. *Geology*, **41**, 1255-1256.

Tonarini S., Pennisim M., Adorni-Braccesi A., Dini A., Ferrara G., Gonfiantini R., Wiedenbeck M. and Gröning M. (2003) Intercomparison of boron isotope concentration measurements. Part I: selection, preparation and homogeneity tests of the intercomparison materials. *Geostandard Newslett*, **27**, 21–39

Tornos F., Wiedenbeck M. and Velasco F. (2012) The boron isotope geochemistry of tourmaline-rich alteration in the IOCG systems of northern Chile: implications for a magmatic-hydrothermal origin. *Miner Deposita*, **47**, 483-499.

Treloar P. J., Lawrence D. M., Senghor D., Boyce A., and Harbidge P. (2015) The Massawa gold deposit, Eastern Senegal, West Africa: an orogenic gold deposit sourced from magmatically derived fluids? *Geological Society London Special Publications*, **393**, 135-160.

Tshibubudze, A., Hein, K.A. and McCuaig, T.C., 2015. The relative and absolute chronology of strato-tectonic events in the Gorom-Gorom granitoid terrane and Oudalan-Gorouol belt, northeast Burkina Faso. *Journal of African Earth Sciences*. [doi:10.1016/j.jafrearsci.2015.04.008](https://doi.org/10.1016/j.jafrearsci.2015.04.008)

van Hinsberg V. J., Henry D. J. and Dutrow B. L. (2011a) Tourmaline as a petrologic forensic mineral: a unique recorder of its geologic past. *Elements*, **7**, 327-332.

van Hinsberg V. J., Henry D. J. and Marschall H. R. (2011b) Tourmaline: an ideal indicator of its host environment. *Can Mineral*, **49**, 1-16.

Vial D.S., Duarte B.P., Fuzikawa K. and Vieira M.B.H. (2007) An epigenetic origin for the Passagem de Mariana gold deposit, Quadrilátero Ferrífero, Minas Gerais, Brazil. *Ore Geol Rev*, **32**, 596-613.

White A., Burgess R., Charnley N., Selby D., Whitehouse M., Robb L. and Waters D. (2014) Constraints on the timing of late-Eburnean metamorphism, gold mineralization and regional exhumation at Damang mine, Ghana. *Precambrian Res*, **243**, 18-38.

Wilson C.J., Schaub P.M. and Leader L.D. (2013) Mineral precipitation in the quartz reefs of the Bendigo gold deposit, Victoria, Australia. *Econ Geol*, **108**, 259-278.

Wyman D.A., Cassidy K.F. and Hollings P. (2016). Orogenic gold and the mineral systems approach: Resolving fact, fiction and fantasy. *Ore Geology Reviews*, **78**, 322-335.

Xavier R.P., Wiedenbeck M., Trumbull R.B., Dreher A.M., Monteiro L.V., Rhede D., De Araujo C.E.G. and Torresi I. (2008) Tourmaline B-isotopes fingerprint marine evaporites as the source of high-salinity ore fluids in iron oxide copper-gold deposits, Carajás Mineral Province (Brazil). *Geology*, **36**, 743-746.

Xue Y., Campbell I., Ireland T.R., Holden P. and Armstrong, R. (2013) No mass-independent sulfur isotope fractionation in auriferous fluids supports a magmatic origin for Archean gold deposits. *Geology*, **41**, 791-794.

Yardley B.W. and Cleverley J.S. (2013) The role of metamorphic fluids in the formation of ore deposits. In *Ore Deposits in an Evolving Earth* (eds. G. R. T. Jenkin, P. A. J. Lusty, I. McDonald, M. P. Smith, A. J. Boyce and J. J. Wilkinson). *Geological Society London Special Publications*, **393**, 117-134.

Yavuz F., Yavuz V. and Sasmaz A. (2006) WinClastour- a Visual Basic program for tourmaline formula calculation and classification. *Comput Geosci*, **32**, 1156-1168.

Figure captions

Fig. 1. Geological sketch map of the Birimian and Archaean terranes in the southern portion of the West African Craton, the location of the study area in the Kédougou-Kéniéba Inlier is indicated.

Fig. 2. (a) Geological sketch map of the Kédougou-Kéniéba Inlier, with major gold deposits highlighted. (b) Geological map of the area surrounding the Senegal-Mali Shear Zone (SMSZ) with studied ore deposits and occurrences highlighted. Tourmaline sample numbers are in parentheses after Au deposit names. Modified after Lawrence et al. (2013a & b) and Lambert-Smith (2015a & b).

Fig. 3. (a) Tourmalinite (tourmalinised quartz wacke) at the Gara deposit, similar units occur throughout the district. Ore phases are hosted in the cross cutting veins. (b) Intensely albitised wall rock at the Yalea deposit, the orange colour is derived from microcrystalline haematite within albite crystals; this style of alteration is present throughout the district. The small intervals on the left of the scale card are cm.

Fig. 4. Geochemical map showing a >200 pm boron anomaly in soil samples from the Kofi Series.

Fig. 5. Hand specimen examples of (a) hydro-fracture ankerite-quartz vein ore with tourmalinised wall rock, and (b) hydrothermal breccia containing tourmaline-carbonate-quartz matrix and cement, and early clasts of tourmalinite. (c) Back scattered electron (BSE) image of early matrix replacive tourmaline in quartz wacke with overprinting auriferous pyrite. (d) Fine grained hydrothermal tourmaline needles protruding from the margin of an auriferous ankerite-quartz-pyrite vein in the Gara ore body, lower BSE image shows the c-axis of a hydrothermal tourmaline needle, note the small spot size achievable with SIMS which enabled analysis of these tourmalines. (e) Subhedral to euhedral hydrothermal tourmaline in the matrix of mineralized hydrothermal breccia. (f) BSE image showing cross section through syn-mineralization breccia hosted tourmaline, showing darker core and lighter rim. (g) BSE image of aggregates of fine grained, subhedral, syn-mineralisation tourmaline at P-64. (h) Fine grained hydrothermal tourmaline replacing auriferous pyrite at the Gara deposit. Ank – ankerite; Py – pyrite; Qtz – quartz; Tur – tourmaline.

Fig. 6. Classification of tourmalines in the Loulo Mining District based on (a) Y- and Z-site occupancy, using the Al-Fe-Mg ternary diagram of Henry and Guidotti, (1985). Fields: (A) Li-rich granitoid pegmatites and aplites; (B) Li-poor granitoids pegmatites and aplites; (C) Fe³⁺-rich quartz-tourmaline rocks (altered

granitoids); (D) metapelites and metapsammites with Al-saturating phase; (E) metapelites and metapsammites lacking Al-saturating phase; (F) Fe³⁺-rich quartz-tourmaline rocks, calc-silicate rocks and metapelites; (G) low-Ca metaultramafic rocks and Cr-V-rich metasediments and; (H) metacarbonates and metapyroxenites. (b) X-site occupancy (after Hawthorne and Henry, 1999).

Fig. 7. Histogram showing the $\delta^{11}\text{B}$ of hydrothermal and magmatic tourmalines analysed from the Loulo Mining District plotted by (a) deposit and (b) tourmaline paragenesis. Pegmatitic $\delta^{11}\text{B}$ data provide constraints on the range of $\delta^{11}\text{B}$ from local magmatism; a detrital tourmaline grain was found within mineralised quartz wackes and displays $\delta^{11}\text{B}$ values equivalent to primary magmatic tourmalines. (c) shows the common $\delta^{11}\text{B}$ compositions of tourmalines hosted in specific lithologies worldwide and (d) the $\delta^{11}\text{B}$ of specific natural reservoirs of B (data from Swihart et al., 1986; Palmer and Slack, 1989; Palmer and Swihart., 1996; van Hinsberg et al., 2011b; Marschall and Jiang, 2011). The +3.7 ‰ arrow represents fluid-tourmaline $\delta^{11}\text{B}$ fractionation at 300 °C (calculated using the equations of Meyer et al., 2008).

Fig. 8. Histogram showing the $\delta^{11}\text{B}$ distribution of the three paragenetic stages of hydrothermal tourmalines growth at the Gara deposit. (a) Early matrix bound tourmaline in altered quartz wacke wall rock (b) Syn-mineralization tourmaline needles in auriferous veins (c) post-mineralization replacive tourmaline overprinting auriferous pyrite. Black lines represent the probability density.

Fig. 9. X-site (a) Na, (b) Ca, and (c) total-X-site occupancy of hydrothermal tourmalines plotted against $\delta^{11}\text{B}$.

Fig. 10. Diagram showing B-isotope fractionation (calculated using the equations of Meyer et al., 2008) between tourmaline and fluid at a range of temperatures between the end member brine and aqueous-carbonic fluids in the Loulo district, with $\delta^{11}\text{B}$ of specific natural reservoirs of B indicated below (data from Swihart et al., 1986; Palmer and Slack, 1989; Palmer and Swihart., 1996; van Hinsberg et al., 2011b).

Fig. 11. Compilation of $\delta^{11}\text{B}$ data from other orogenic gold deposits, compared against $\delta^{11}\text{B}$ in tourmalines hosted in specific geological settings. Data are from Jiang et al. (2002); Krientiz et al. (2008); Baksheev et al. (2014), Beaudoin et al., (2013), and Molnar et al. (2016).

Tables

Table 1. Selected mineral chemical data from EDS analyses of hydrothermal tourmalines of different paragenetic stages in the LBD. Structural formulae were calculated using the Winclastour software of Yauz et al. (2006).

Table 2. Boron isotope analysis of hydrothermal and magmatic tourmalines from the Loulo Mining District and Falémé Volcanic Belt.

Table1

Paragenesis	Early												Syn-ore			Replacement		
Location	Baqata		Gara		Yalea	F-64		Yalea	Gara	LD27-1	Gara		LD44-6					
Sample-spot#	BP1204-6	BP1204-8	LD44-7	PT7-3A	YD82-2	PT10-4	PT10-10	YD82-9A	LD44-4	LD27-1	LD27-5	LD44-5	LD44-6					
SiO ₂	37.12	37.25	38.53	37.06	35.44	37.23	37.50	38.29	38.32	37.21	36.90	38.05	36.89					
TiO ₂	0.72	0.52	-	0.71	0.24	-	-	-	-	0.41	0.22	0.55	-					
Al ₂ O ₃	30.49	30.29	30.86	28.92	26.76	31.11	30.79	28.06	31.77	30.89	31.96	30.25	32.42					
FeO	2.89	3.79	5.55	5.97	9.59	5.49	6.45	8.56	7.43	5.59	3.79	6.14	8.92					
MgO	10.72	10.17	8.69	9.47	8.50	9.37	8.64	8.61	6.45	9.02	10.09	8.50	5.89					
CaO	0.51	0.60	-	0.61	0.19	-	-	-	-	0.31	0.28	0.29	-					
Na ₂ O	2.56	2.45	2.56	2.57	2.82	2.67	2.21	2.56	2.13	2.28	2.64	2.25	1.98					
H ₂ O(c)	3.58	3.56	3.52	3.57	3.48	3.55	3.40	3.48	3.37	3.47	3.60	3.46	3.31					
B ₂ O ₃ (c)	10.66	10.62	10.72	10.52	10.18	10.71	10.67	10.58	10.61	10.67	10.77	10.65	10.58					
Total	99.25	99.25	100.43	99.40	97.20	100.13	99.66	100.13	100.08	99.85	100.25	100.14	100.00					
	normalised to 15 cations (T + Z + Y)																	
Si (atoms per formula unit; apfu)	6.05	6.10	6.25	6.12	6.05	6.04	6.11	6.29	6.28	6.06	5.96	6.21	6.06					
Ti	0.09	0.06	-	0.09	0.03	-	-	-	-	0.05	0.03	0.07	-					
Al	5.86	5.84	5.90	5.63	5.39	5.95	5.91	5.43	6.13	5.93	6.08	5.82	6.28					
Fe ²⁺	0.39	0.52	0.75	0.83	1.37	0.75	0.88	0.89	1.02	0.76	0.51	0.84	1.23					
Mg	2.61	2.48	2.10	2.33	2.16	2.27	2.10	2.11	1.58	2.19	2.43	2.07	1.44					
Ca	0.09	0.11	-	0.11	0.04	-	-	-	-	0.05	0.05	0.05	-					
Na	0.81	0.78	0.81	0.82	0.93	0.84	0.70	0.82	0.68	0.72	0.83	0.71	0.63					
B	2.99	2.99	2.99	3.00	3.02	3.01	3.01	3.01	2.98	3.00	3.00	2.99	3.00					
Al _z	5.44	5.40	5.90	5.23	5.00	5.34	5.35	5.15	6.00	5.38	5.45	5.82	5.53					
Mg _z	0.56	0.60	0.10	0.77	1.00	0.66	0.65	0.85	0.00	0.62	0.55	0.18	0.48					
Total Z	6	6	6	6	6	6	6	6	6	6	6	6	6					
Al _y	0.42	0.44	-	0.40	0.38	0.61	0.56	0.28	0.13	0.55	0.59	-	0.75					
Ti _y	0.09	0.06	-	0.09	0.03	-	-	-	-	0.05	0.03	0.07	-					
Mg _y	2.04	1.88	2.00	1.56	1.17	1.61	1.45	1.25	1.58	1.57	1.88	1.89	0.97					
Fe ²⁺ _y	0.39	0.52	0.75	0.83	1.37	0.75	0.88	0.89	1.02	0.76	0.51	0.84	1.23					
Total Y	2.95	2.91	2.75	2.88	2.95	2.96	2.89	2.71	2.72	2.94	3.00	2.79	2.94					
Ca _x	0.09	0.11	-	0.11	0.04	-	-	-	-	0.05	0.05	0.05	-					
Na _x	0.81	0.78	0.81	0.82	0.93	0.84	0.70	0.82	0.68	0.72	0.83	0.71	0.63					
Total X	0.90	0.88	0.81	0.93	0.97	0.84	0.70	0.82	0.68	0.78	0.87	0.76	0.63					
X-vac.	0.10	0.12	0.20	0.07	0.03	0.16	0.30	0.19	0.32	0.23	0.13	0.24	0.37					

Note - (c) indicates calculated weight % data; subscript letters denote structural sites; - indicates concentrations below the detection limits of the EDS method.

Table2

Location	Sample-spot#	Paragenesis	$^{11}\text{B}/^{10}\text{B}$	$\delta^{11}\text{B}$ (‰)	1σ (‰) ^a
<i>Hydrothermal tourmaline</i>					
Baqata	BP1204-1	Early matrix	4.099	13.6	0.54
	BP1204-2	Early matrix	4.101	14.3	0.43
	BP1204-3	Early matrix	4.108	15.9	0.47
	BP1204-4	Early matrix	4.099	13.7	0.61
	BP1204-5A	Early matrix	4.096	13.0	0.56
	BP1204-6	Early matrix	4.1	14.0	0.72
	BP1204-8	Early matrix	4.097	13.3	0.47
	BP1204-9	Early matrix	4.1	13.9	0.53
	BP1204-10	Early matrix	4.1	14.0	0.69
	Gara	LD27-1	Replacement	4.064	5.1
LD27-2A		Replacement	4.073	7.2	0.46
LD27-2B		Replacement	4.082	9.5	0.43
LD27-5		Replacement	4.105	15.1	0.43
LD27-5B		Replacement	4.075	7.7	0.45
LD27-10A		Replacement	4.044	0.0	0.49
LD27-10B		Replacement	4.059	3.7	0.45
LD27-10C		Replacement	4.085	10.1	0.53
LD27-10D		Replacement	4.055	2.8	0.4
LD27-10E		Replacement	4.05	1.6	0.61
LD27-10F		Replacement	4.049	1.2	0.41
LD44-1		Syn-ore needles	4.061	4.3	0.72
LD44-2		Syn-ore needles	4.059	3.8	0.73
LD44-4		Syn-ore needles	4.071	6.9	0.57
LD44-5		Replacement	4.053	2.2	0.82
LD44-6		Replacement	4.043	-0.3	0.67
LD44-7		Early matrix	4.083	9.7	0.53
LD44-8		Replacement	4.063	4.9	0.65
LD44-11		Early matrix	4.076	8.0	0.66
PT7-1		Early matrix	4.085	10.1	0.5
PT7-1A		Early matrix	4.094	12.4	0.48
PT7-1B		Early matrix	4.094	12.4	0.47
PT7-3		Early matrix	4.111	16.7	0.55
PT7-3A		Early matrix	4.11	16.3	0.42
PT7-3B		Early matrix	4.085	10.1	0.69
PT7-4		Early matrix	4.095	12.7	0.51
PT7-5		Detrital	3.984	-14.8	0.6
PT7-5A		Detrital	3.978	-16.1	0.55
PT7-5B		Early matrix	4.095	12.7	0.53
PT7-7		Early matrix	4.111	16.6	0.54
PT7-7A		Early matrix	4.104	15.0	0.54
P-64		PT10-1	Syn-ore	4.043	-0.3
	PT10-2	Syn-ore	4.042	-0.3	0.49
	PT10-3	Syn-ore	4.035	-2.2	0.56
	PT10-4	Syn-ore	4.048	1.0	0.51

Figure_1

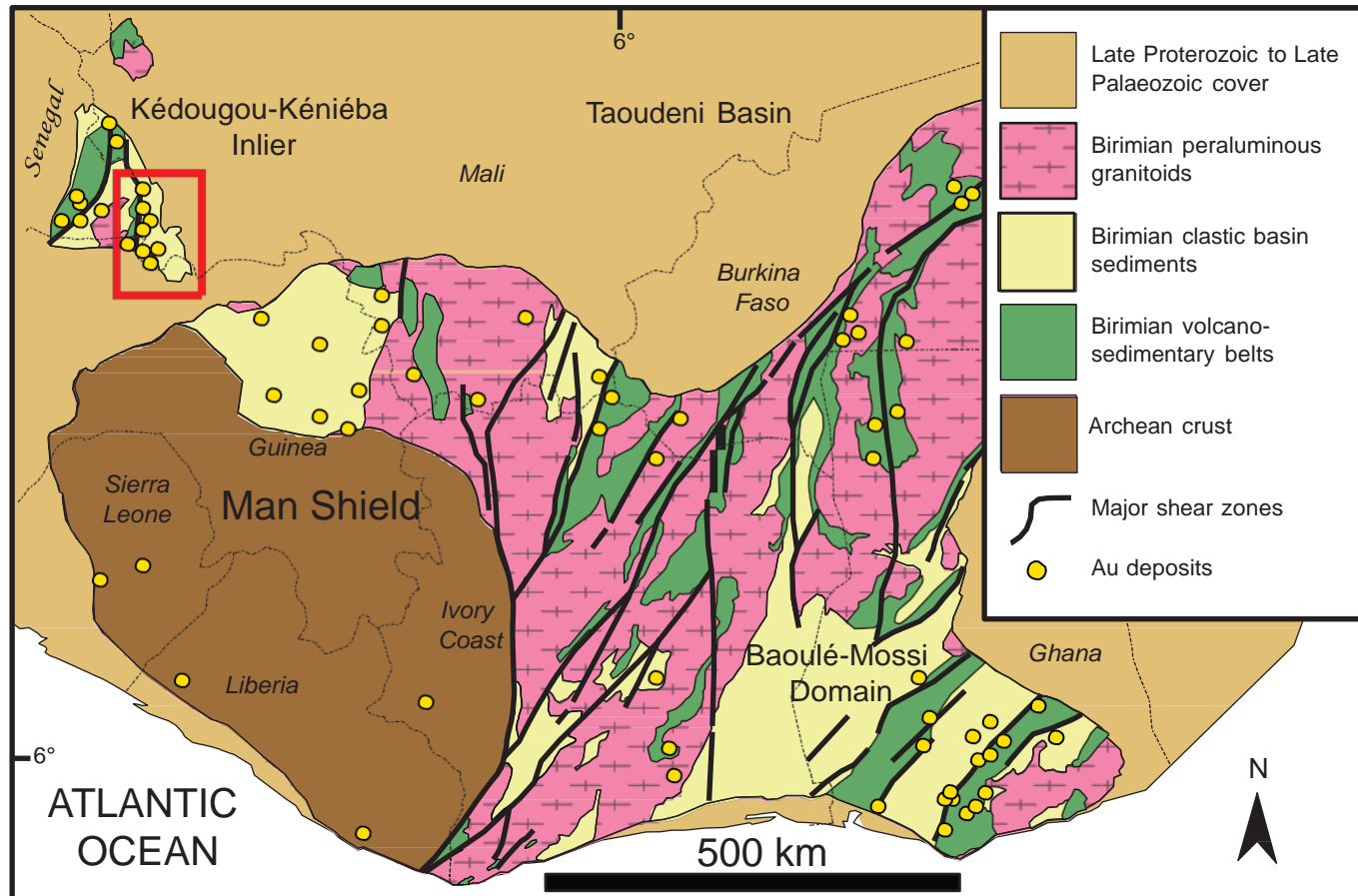
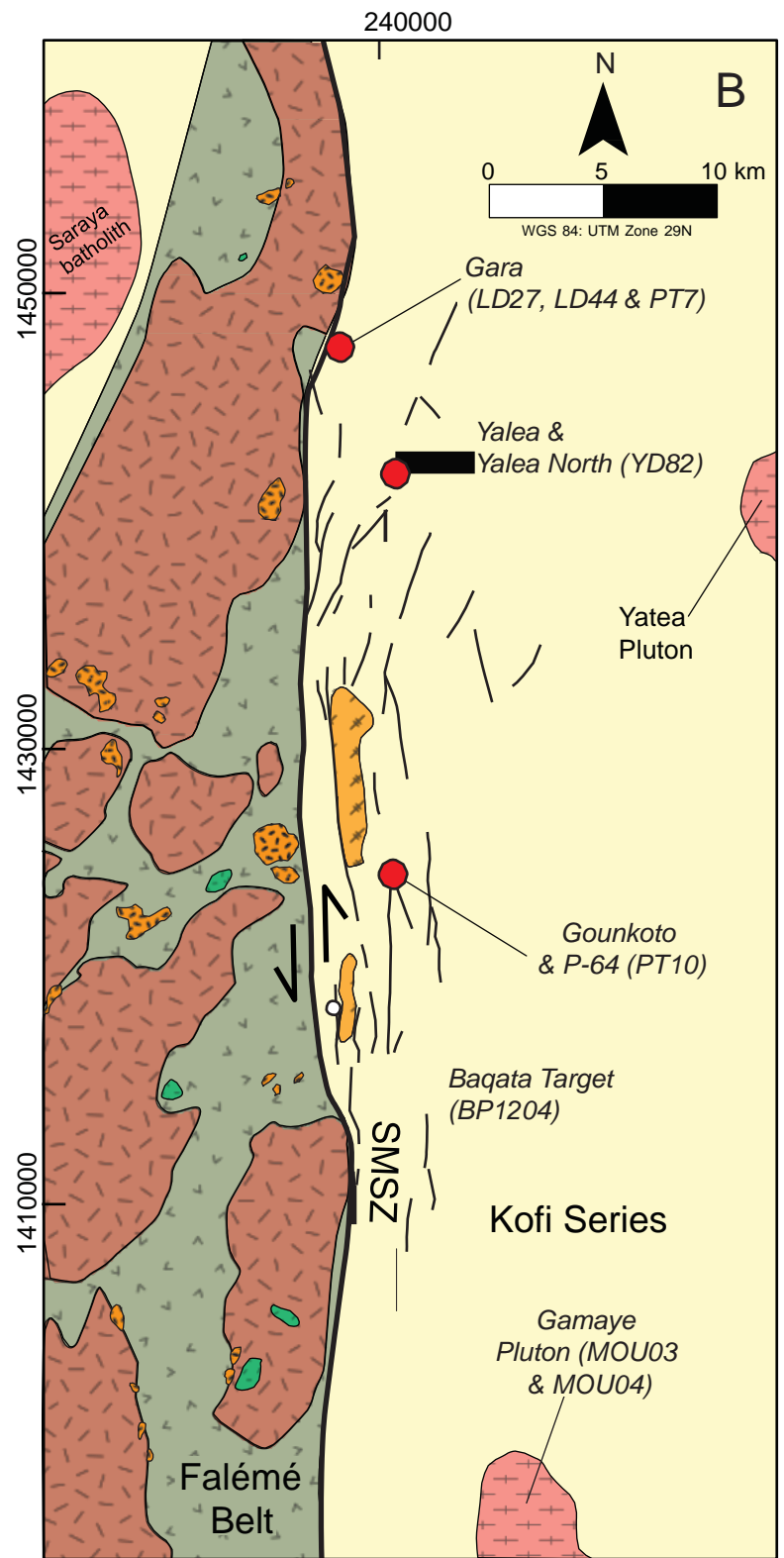
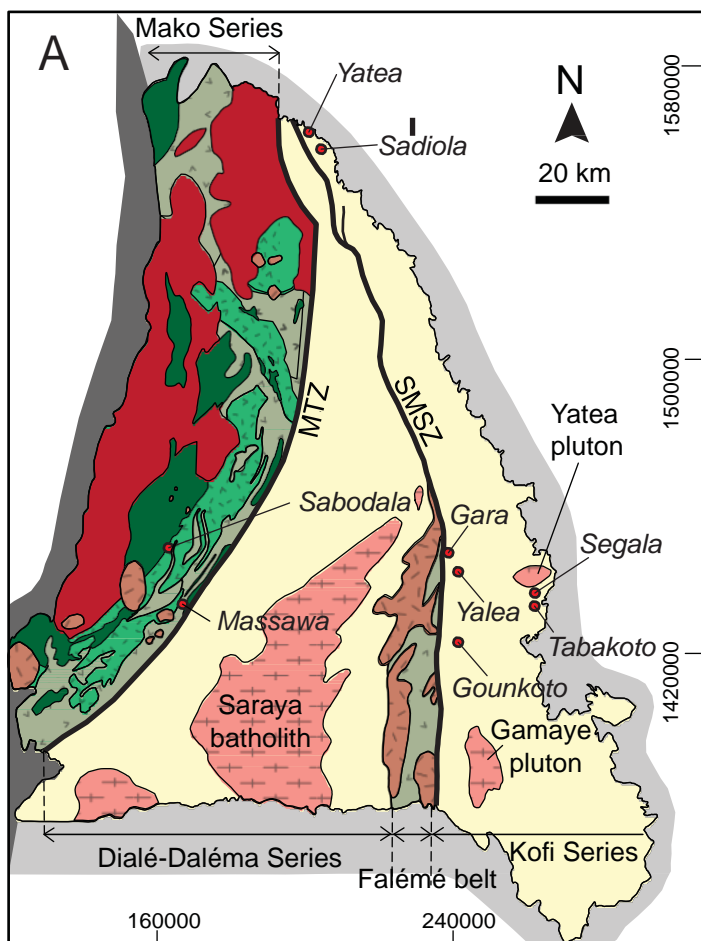


Figure 2



Legend

Cover sequences

- Neoproterozoic Taudeni Basin
- Mauritanides (Hercynian mobile belt)

Birimian lithologies

- Hydrothermal albitite
- Peraluminous monzogranite and granite
- Kofi Series metasedimentary rocks
- Dioritic to monzonitic, metaluminous calc-alkaline rocks
- Volcaniclastic sediments and carbonate rocks
- Calc-alkaline lavas volcanic rocks
- Tholeiitic basalts
- Kakadian Batholith

Map symbols

- Major shear zone
- Shear zone (Inferred)
- Au mine
- Magnetite skarn mineralisation
- SMSZ - Senegal-Mali Shear Zone
- MTZ - Main Transcurrent Zone

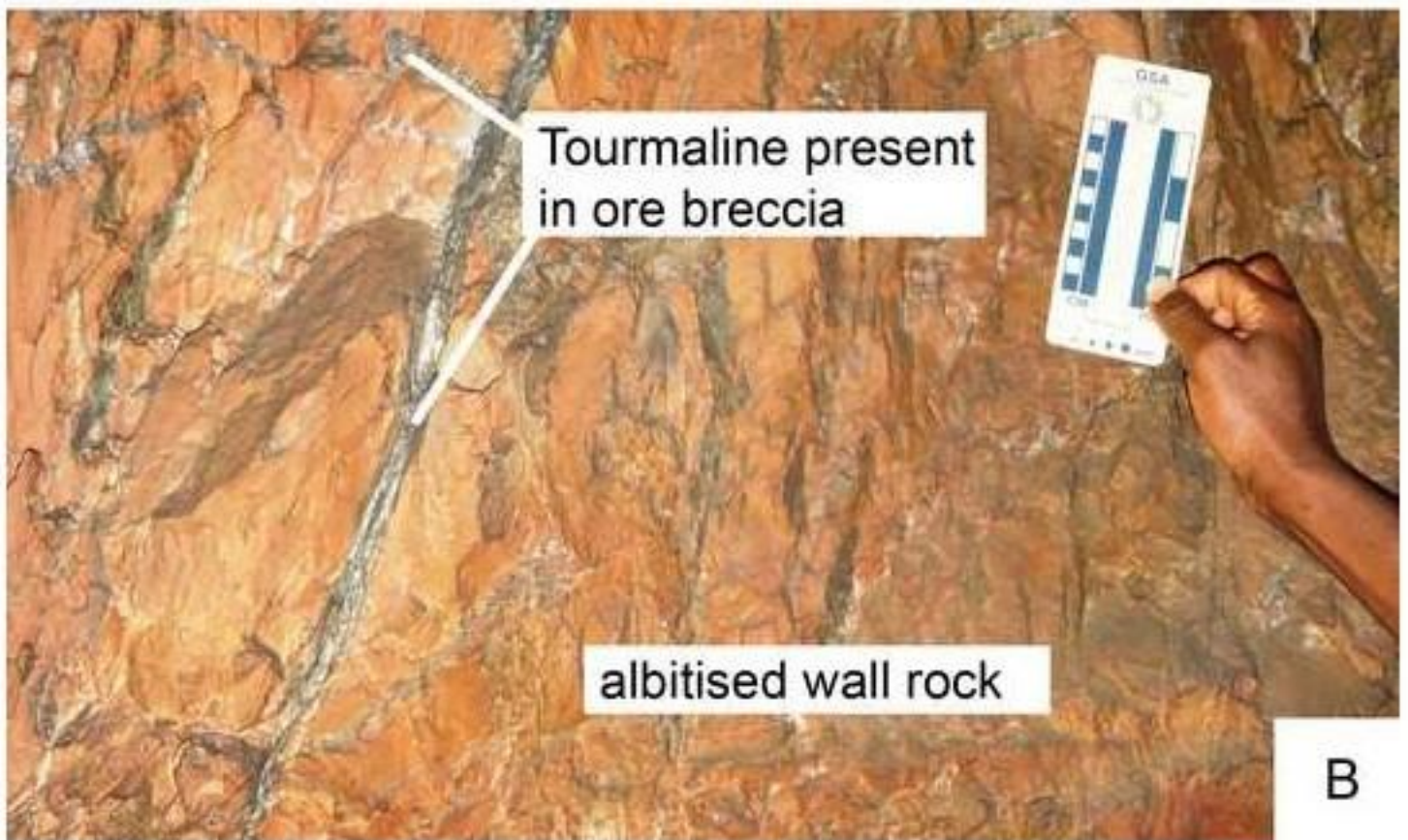
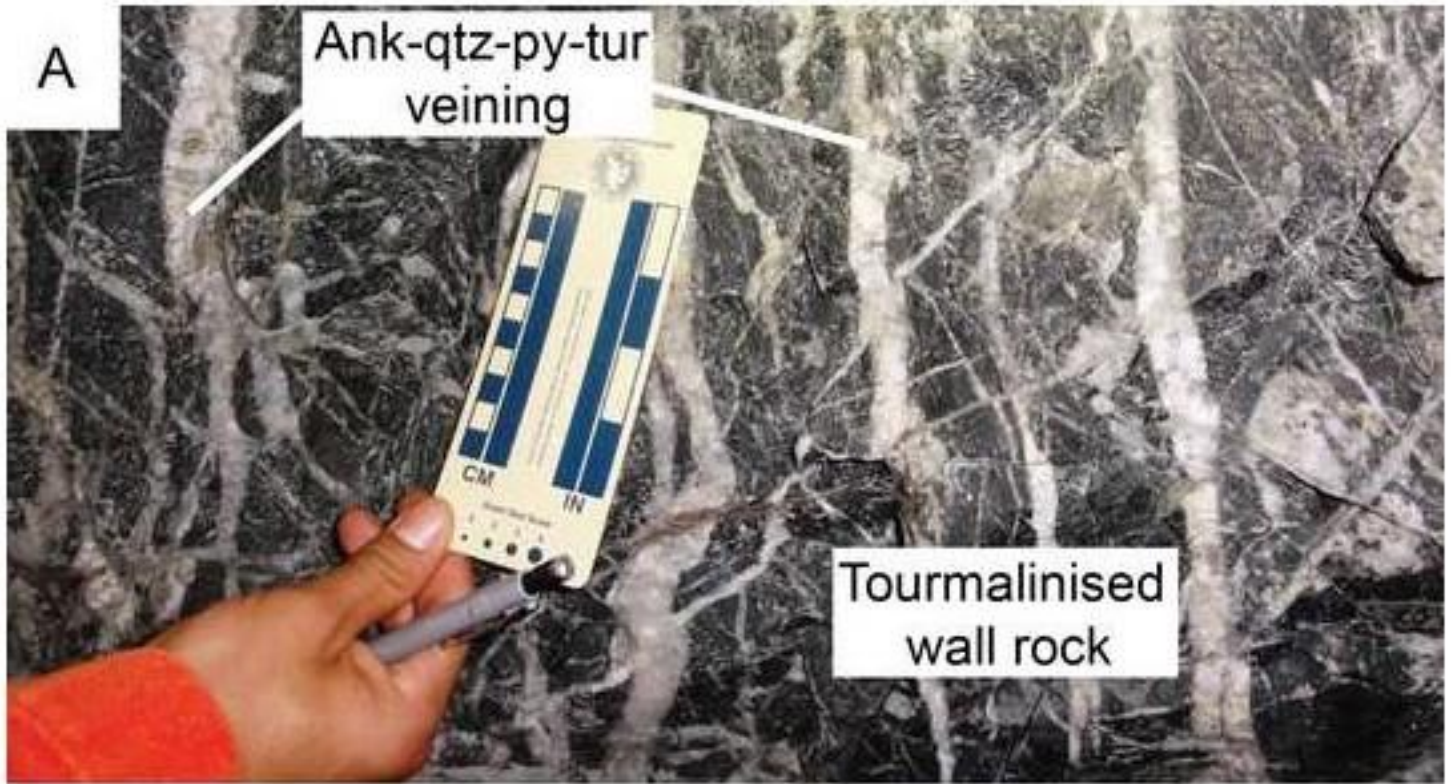


Figure_4

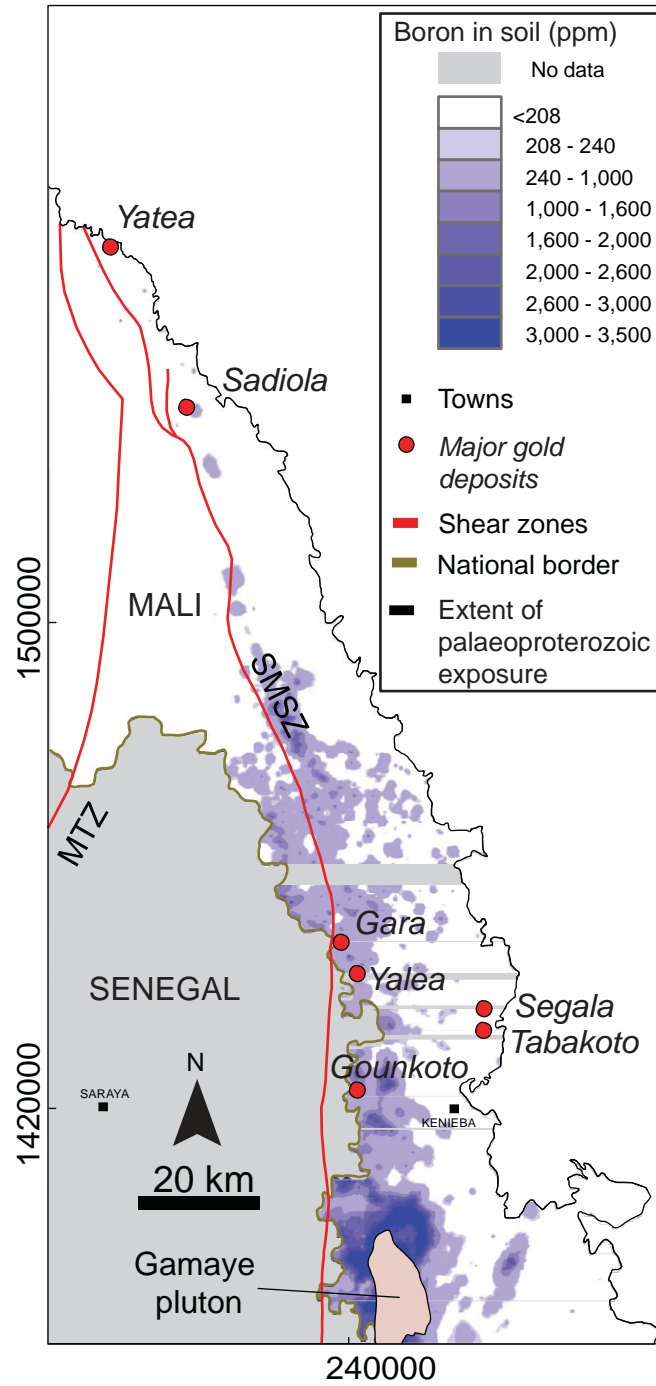


Figure_5

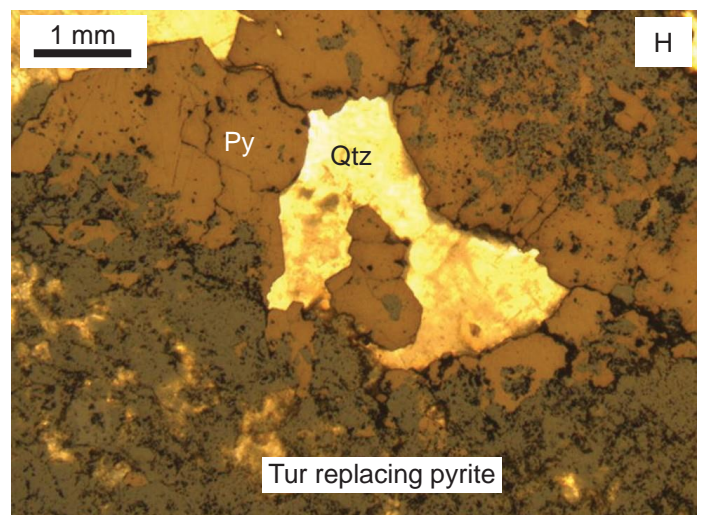
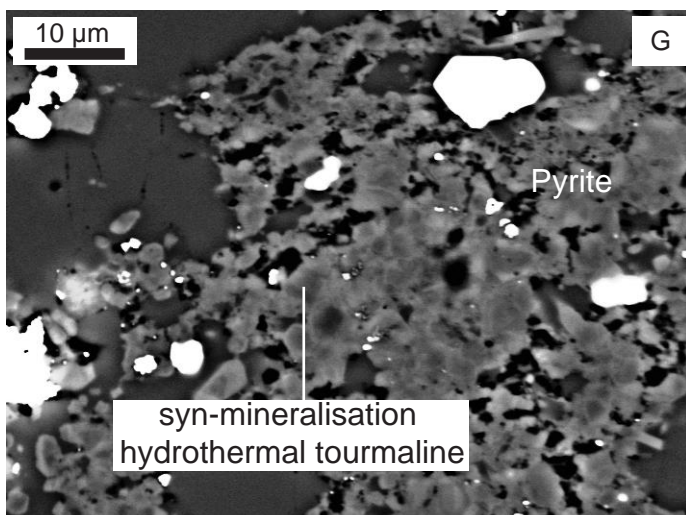
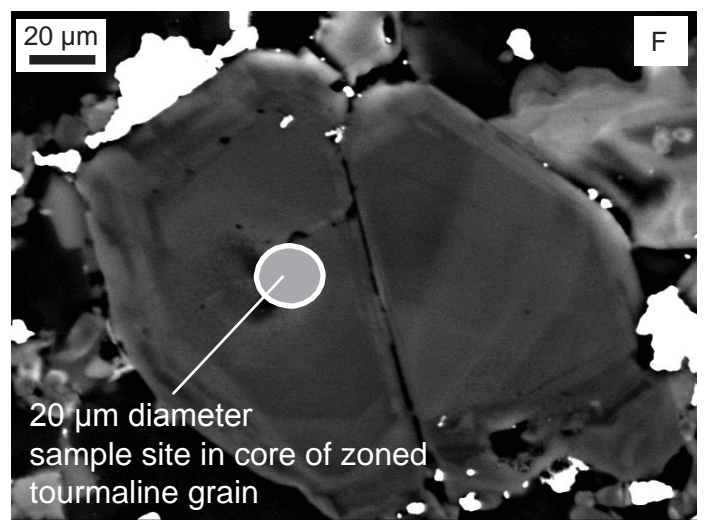
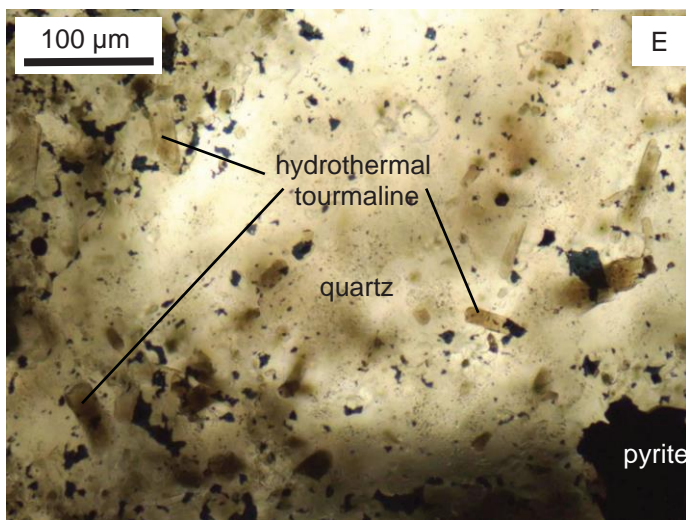
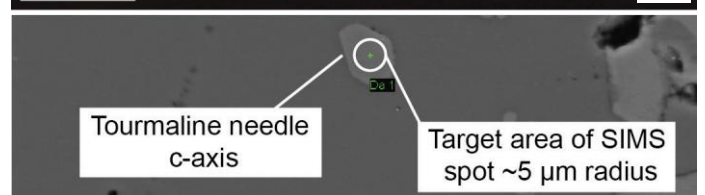
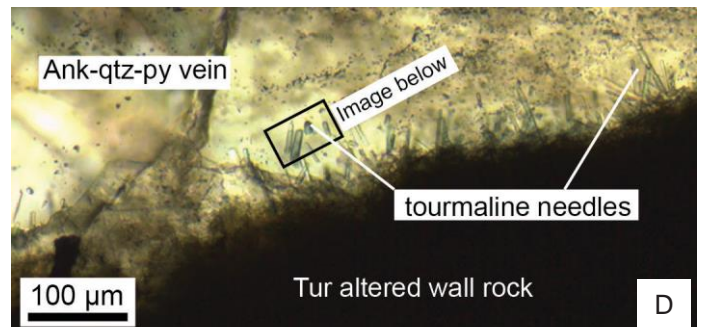
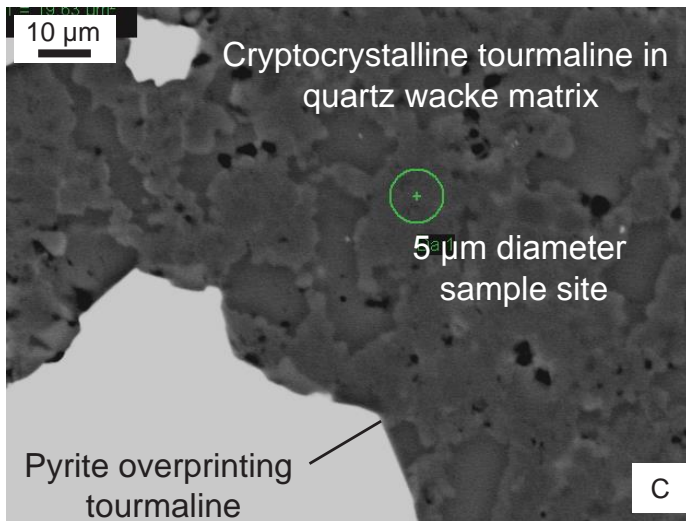
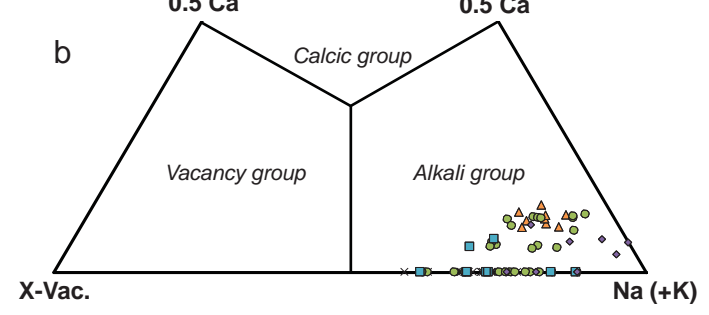
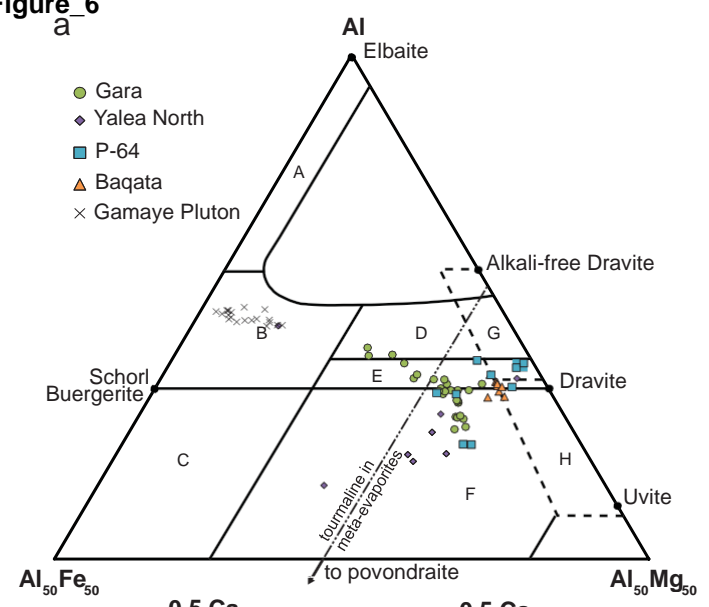
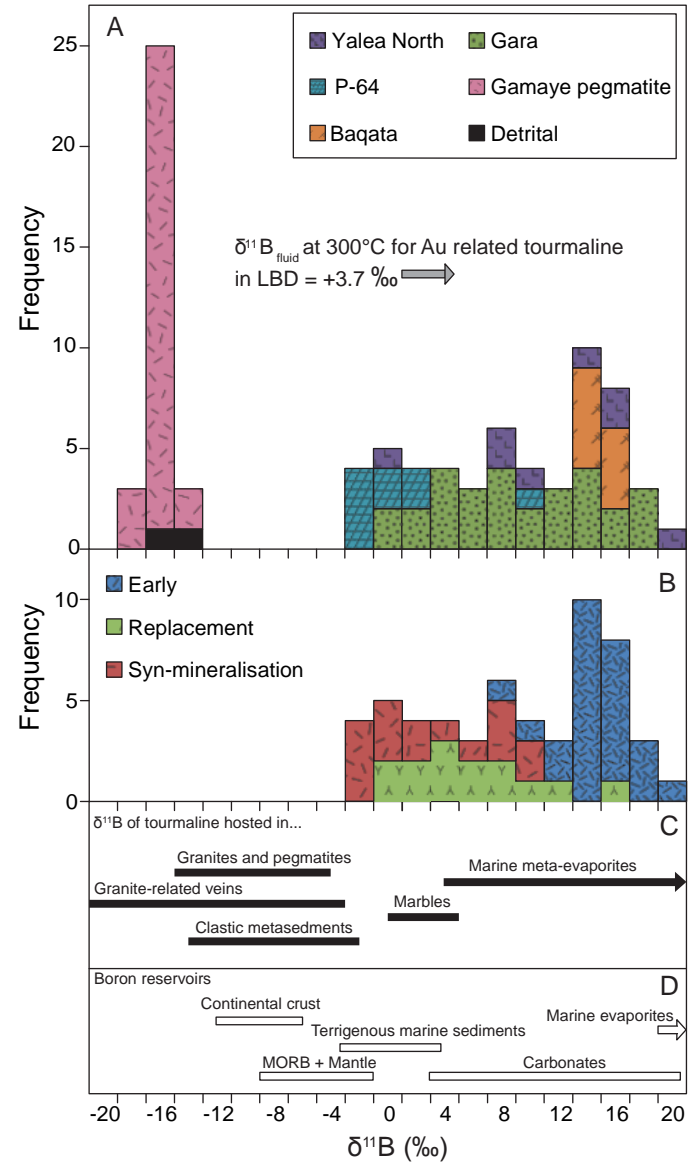


Figure 6



Figure_7



Figure_8

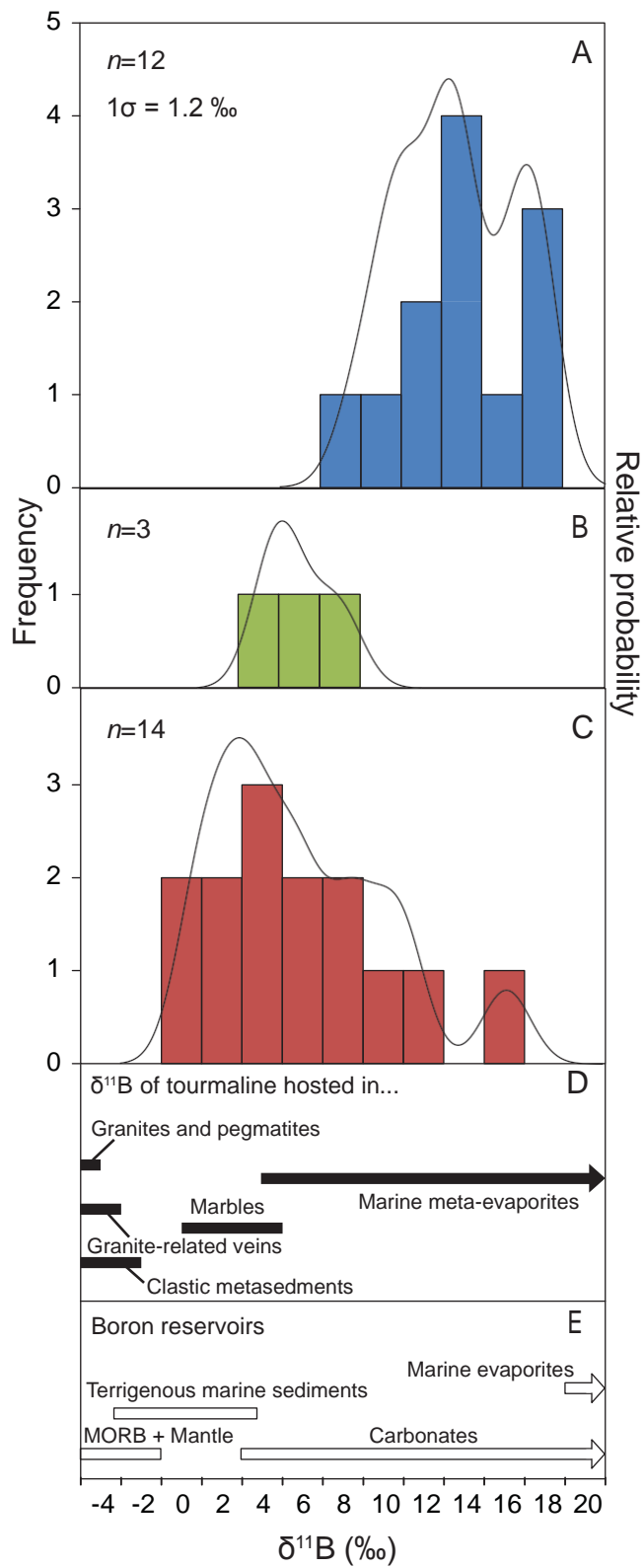


Figure_9

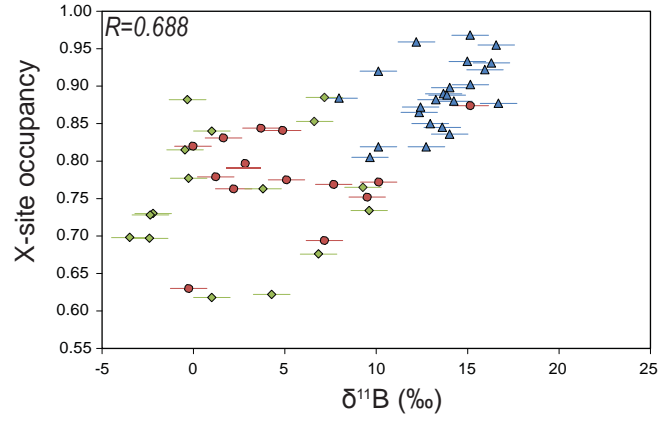
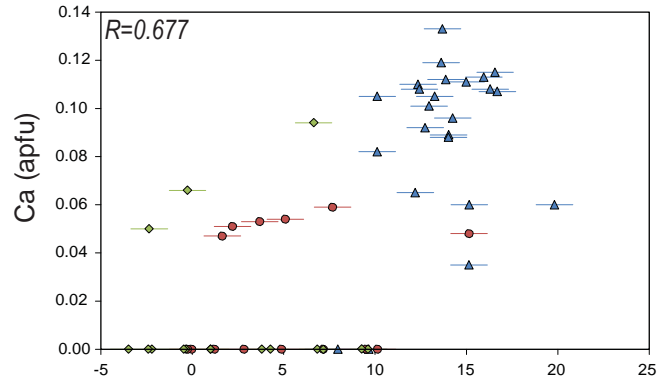
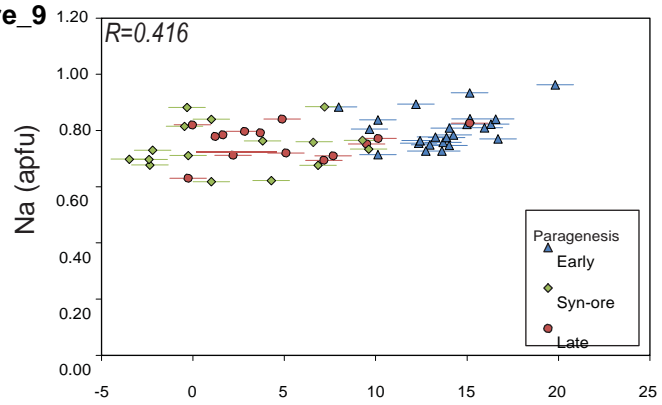


Figure_10

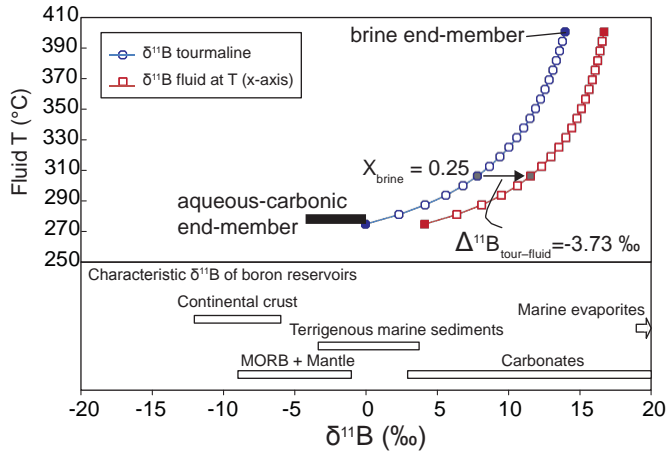


Figure_11

